
Load transfer mechanism of an unwelded, unbolted, grouted connection for prefabricated composite columns under axial loads

Lili SUI^{1,2}, Shiyong FAN^{1,2}, Zhenyu HUANG^{*1,2}, Wei ZHANG^{1,2}, Jianqiao Ye³

¹Guangdong Provincial Key Laboratory of Durability of Marine Civil Engineering, Shenzhen University, Shenzhen 518060, China

²College of Civil and Transportation Engineering, Shenzhen University, Shenzhen 518060, China

³Department of Engineering, Lancaster University, Lancaster, LA1 4YR, UK

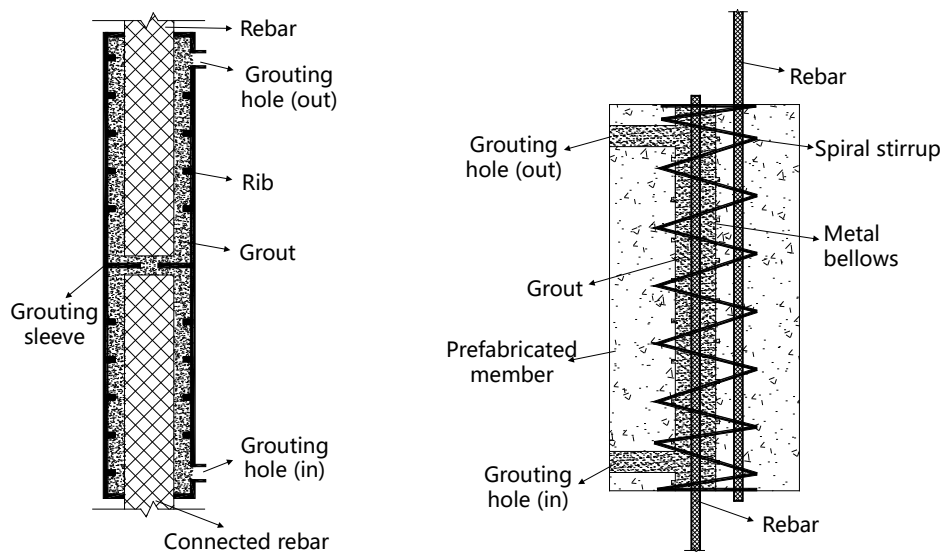
Abstract

This study develops a novel unwelded, unbolted, ultrahigh-performance fibre-reinforced concrete (UHPFRC) grouted connection for prefabricated square tubular composite columns. Herein, eight full-scale columns with UHPFRC grouted connections are tested to investigate their ultimate tensile and compressive resistance. The test results show that the novel connections exhibit good resistance and structural stiffness. The primary failure modes are punching shear of the end plate, welding fracture at the inner tube, tube yielding and local buckling of the steel tube. The test specimens are simulated using finite element analysis in ABAQUS. The experimental and simulated results are in good agreement, indicating that the FE simulations can capture the observed failure modes and ultimate resistance. Thereafter, existing analytical design formulas are evaluated to assess their suitability to predict the compressive and tensile resistance of prefabricated tubes with/without the novel grouted connections. A good agreement between the formula predictions and the test results are observed. These analytical formulas have the potential to be used in the design of the novel unwelded, unbolted, UHPFRC grouted connections for prefabricated steel, reinforced concrete and steel-concrete composite columns.

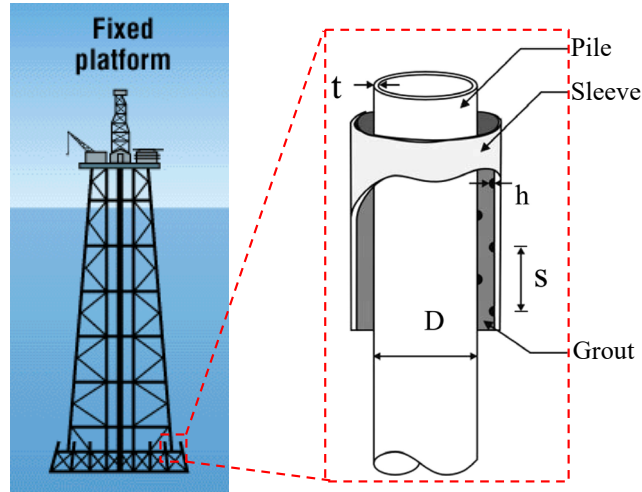
Keywords: Grouted connection; Square steel tubular column; Numerical simulation; UHPFRC.

1. Introduction

Prefabricated building structures consist of prefabricated parts that are assembled on construction sites. Compared with the traditional building structures (e.g., cast in situ reinforced concrete (RC) structures), prefabricated building structures have a range of advantages, including increased construction productivity and quality, reduced labour, and decreased energy consumption and carbon emissions. These advantages promote green construction, which will be a major trend in the future development of the building construction industry [1-2]. With the increasing demand for housing and the growing capacity of manufacturing in China, industrialization of construction provides a very attractive and cost-efficient alternative in shaping the current and future infrastructure [3,4]. Studies of precast concrete and prefabricated building structures have been widely used in Europe, the United States, Japan and other international regions. The connections between the prefabricated structural components are always of special concern in the assembly of prefabricated constructions. The safety and reliability of the connections directly affect the overall structural performance of the assembled structures. The existing studies have mainly focused on various joints in traditional RC structures and steel structures, such as cast in situ concrete joints [5], bolted connections [6] and welded connections [7]. These prefabricated components are normally prepared in a factory environment and assembled on-site, which still requires significant on-site building work due to the numerous structural components.



(a) Grouted reinforcement sleeve connection and (b) grouted anchor connection



(c) Pile sleeve connection [35]

Figure 1. Grouted connection for RC structures and offshore structures

At present, the commonly used connections in prefabricated RC structures are grouted reinforcement sleeve connections (Figure 1a) and grouted anchor connections (Figure 1b). The grouted sleeve connection is a key technology in prefabricated RC structures. The rebars are inserted into the sleeve that is grouted with high-strength, expansive cement. This connection provides high shear strength that transfers the force from the upper rebar to the lower rebar. This technology has been widely used in the United States and Japan and has been constantly improved through continuous experimental research and practical engineering tests. The connection technology is also recommended for the design code of high-rise prefabricated buildings (JGJ1-2014) [8]. In recent years, there has been more research on grouted reinforcement sleeves [9-14]. Ling et al. [9] and Wu et al. [10] investigated the failure patterns and load-displacement relations of grouted steel sleeve joints, in which they particularly focused on the rebar embedment length and diameter. Under active confinement, the required embedment depth of the rebar can be reduced to 8 times of the rebar diameter. The failure process of the grouted sleeve is similar to the stress-strain relation of a steel rebar. Zheng et al. [13] proposed a new grouted deformed pipe splice (GDPS) sleeve, and the tests on the GDPS sleeve showed good tensile capacity that satisfied the requirements in JGJ107-2016 [15]. However, the new GDPS sleeve requires a special fabrication process and higher installation accuracy, leading to a higher cost than the conventional steel sleeves. To study the effect of the sleeve cavity on the bond behaviour of the grouted sleeve connection, Zheng et al. [14] carried out an axial

tensile test, taking into account the number, spacing and height of the ribs of the sleeve. Their results showed that increasing the number and the height of ribs significantly increased the tensile capacity and the stiffness of the grouted sleeve connection before yielding. Based on the abovementioned studies, the grouted steel bar sleeve connections performed well in terms of their tensile and deformation capacity when joining steel rebars. Unfortunately, at present, there are still problems that need to be addressed in order to promote wider applications of the emerging joint technology. These include that (1) the properties of sleeve and grouting materials in the market vary and are not properly regulated; (2) there is a shortage of skilled labour to do adequate grouting, and (3) there is a lack of relevant technical standards. The current sleeve connections still require significant on-site operations, leading to low construction efficiency and a poor construction environment, which may also introduce substantial safety risks for structural members in high-rise buildings. Therefore, the demand for new types of connections that are simple and can be rapidly constructed for prefabricated buildings is highly urgent.

Pile sleeve is another type of grouted connection that is used in the offshore engineering practice to assemble heavy platform structures and pile foundations, aiming to reduce installation inaccuracy and eliminate on-site bolting and welding, which significantly simplifies the complexity of platform construction process even in an extreme construction environment [16]. This grouted connection can be described as a composite connection consisting of high strength grout cast in an annulus between two concentric circular tubes with different diameters, as shown in Figure 1c. To enhance shear transfer, shear keys in the form of ribs are always welded to the surface of the steel tubes. As this is a simple, rapid installation technique, in a harsh marine environment, the grouted connection has been widely used in offshore structures to connect pile foundations and transition pieces of offshore wind turbines. Billington et al. [17] first carried out a large number of tests on this type of grouted connection and found that the connections with a shear key exhibit much higher axial bearing capacity than those without. The findings suggested that the grout properties and the connection size have a great impact on the ultimate resistance. Subsequently, the United States, Japan, Australia and other countries conducted systematic research on this connection technology [18-22]. Karsan and Krahl [23] proposed the calculation formula to predict the shear resistance of grouted connections and compiled it into the API code [24]. Accordingly, design guidelines,

such as the DOE code [25] in the United States and the DNV codes [26, 27] in Norway, have also published design methods for grouted connections. These specifications significantly contribute to the development of the ultimate resistance design approaches for grouted steel pile sleeves. A typical design of such may consider a wide range of design parameters, including the form of the shear key, the stiffness of the sleeve, the material properties of the grout, the height-distance ratio of the shear key (h/s), the thickness-distance ratio (b/s) of the grout, and the aspect ratio of the connection [28-30]. Unfortunately, only a few research efforts have been made for grouted connections of other section forms, such as rectangular hollow sections (RHSs) and square hollow sections (SHSs). Thus, the mechanical behaviour of these grouted sections remains unclear. For non-marine building structures, columns are mainly made in the form of RHSs and SHSs since these components are more effective and efficient for on-site assembly and architectural arrangement [31]. This study develops a new type of grouted ultrahigh-performance fibre-reinforced concrete (UHPFRC) connection for prefabricated SHS and RHS steel and steel-concrete composite columns. This new connection provides great superiority in fabrication and construction by removing the necessity for welding and bolting and considerably decreasing the number of member connections, on-site labour and additional construction requirements. Compared to the normal cast in situ concrete used in the traditional column connections, UHPFRC, which has high tensile strength and ductility, can provide a high shear strength even after cracking [32-34]. In addition, due to the existence of steel fibres, the shrinkage deformation of UHPFRC can also be controlled so that the effective bond strength between the grout and tube can be enhanced [35].

Through combined experimental and numerical studies, this study aims to reveal the load transfer mechanism and mechanical behaviour of the innovative UHPFRC grouted connection under uniaxial tensile and compressive loads. The development of the UHPFRC and material tests are first presented, followed by tensile and compressive tests of eight full-scale SHS tubes with/without the grouted connection to show the failure modes and the load-deformation relationship of the specimens. A finite element (FE) model is established to investigate the failure process. Analytical models are finally evaluated to provide a better understanding of the failure mechanism and ultimate resistance, thereby serving as a guide for the design of the novel UHPFRC grouted connections for prefabricated steel, RC and steel-concrete composite

columns.

2. Full-Scale Experiments

This section details the novel UHPFRC grouted connection for an SHS composite column without any welding or bolting. Figure 2 illustrates the concept, the prefabrication and the assembly process of the UHPFRC grouted connection, in which the upper and lower steel tubes are prepared by welding the shear keys on the outside surface of the inner tube and inside surface of the upper tube, respectively. Afterwards, the upper and lower steel tubes are precisely assembled on-site before grouting UHPFRC using the grouting hole on the upper tube, resulting in a novel unwelded, unbolted connection for steel, RC or steel-concrete composite columns.

This section conducts full-scale experiments to investigate the tensile and compressive behaviour of the SHS tubular column connections. Some researchers have adopted simplified methods, such as the direct double shear test, to calculate the shear capacity of large-diameter grouted connections [22, 29, 36]. These simplified methods can be effectively implemented in the tests when the laboratory environment is limited and the failure modes are easy to observe. However, these research findings from component tests cannot represent the structural stiffness and ultimate resistance behaviour of the full-scale system, which may not be applied directly in practical design [37]. In this case, a full-scale experiment should provide a more accurate result for realistic engineering design purposes.

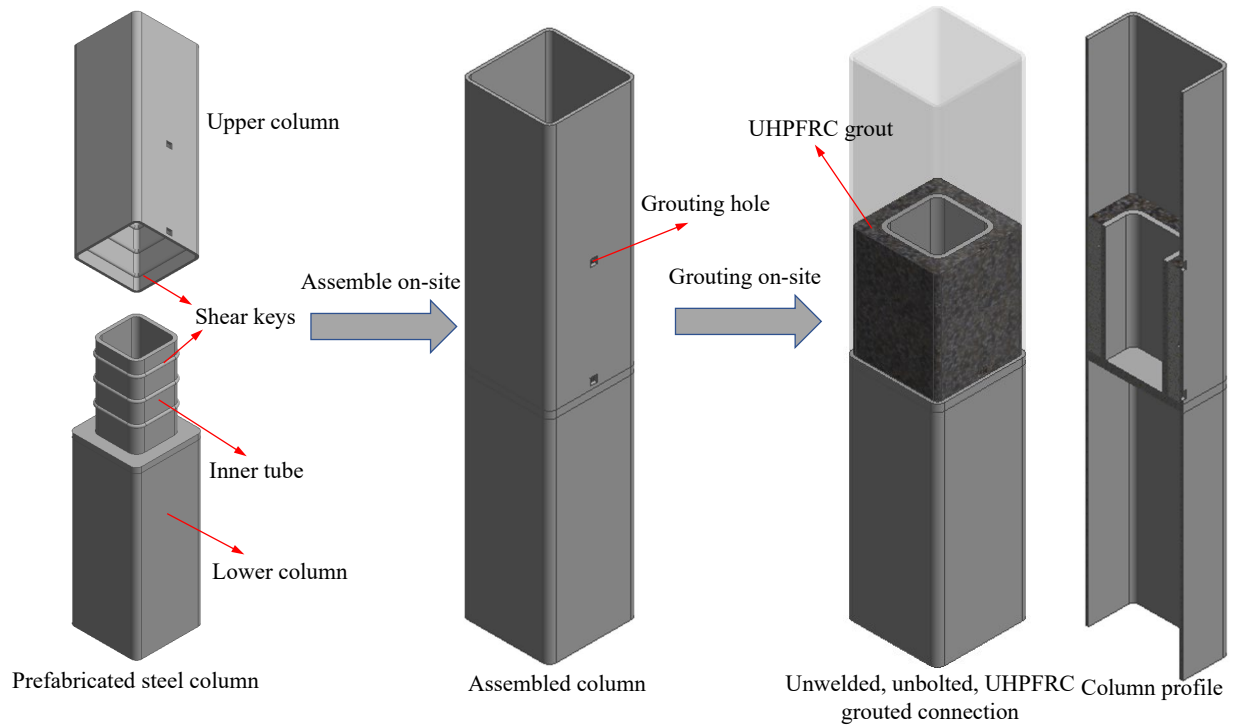


Figure 2. Development of novel unwelded, unbolted UHPFRC grouted connection for composite columns

2.1 Materials

2.1.1 Development of UHPFRC

The new UHPFRC consists of ultrafine silica fume (SF), granulated ground blast furnace slag (GGBFS), PII 52.5 R Portland cement, fine sand, sugar calcium retarder and 2% steel fibres. Table 1 lists the characteristic parameters of the steel fibres. Table 2 lists the mix proportion of the UHPFRC.

Table 1. Steel fibre characteristic parameters

Fibre type	Tensile strength (MPa)	Elastic modulus (GPa)	Length (mm)	Diameter (mm)	Length to diameter ratio	Density ($\text{kg}\cdot\text{m}^{-3}$)
Steel fibre	2750±15%	200	13±10%	0.21±10%	62±15%	7850

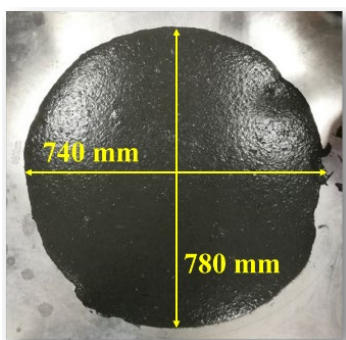
Table 2. Mix proportion of UHPFRC (kg/m^3)

Mix	W/B	W	OPC	SF	GGBFS	S	F	HWRA	SRA	Retarder
UHPFRC	0.14	174.3	967.6	154.8	190.9	927.5	156	33.3	5.39	1.97

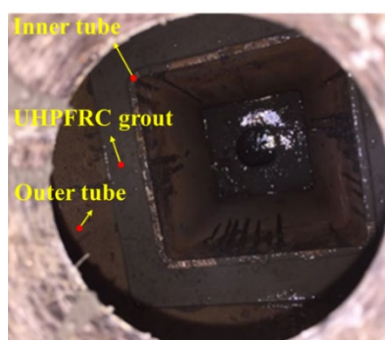
*W/B=water to binder ratio; W=water; OPC=ordinary Portland cement; SF=silica fume; GGBFS= ground granulated blast furnace slag; S=sand; F=steel fibre; HWRA=high water reducing agent; SRA=shrinkage reducing agent; R=retarder.

Two forced-type twin-shaft concrete mixers were used simultaneously to produce the UHPFRC. First, all the dry blending components, including the OPC, SF, GGBFS and sand, were slowly mixed in the mixer

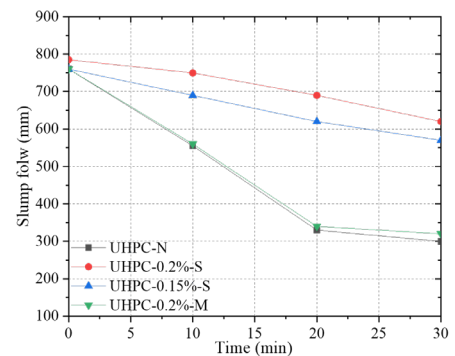
for 2 min until a homogeneous dry mixture was achieved. Then, water was added, and the superplasticizer was gradually poured into the mixer. After the surface of the powder appeared slightly wet and the mixture showed a fluidized state, the steel fibres were evenly added, and the mixture was mixed for a minimum of 5 minutes to obtain a uniform distribution of the steel fibres in the fresh grout. The UHPFRC had a satisfactory consistency in its fresh state, with an average measured slump flow of 760 mm (Figure 3a), according to ASTM C1611-2014 [38], before being placed into the steel formwork, as shown in Figure 3b. Since the setting time for the UHPFRC grout to reach a hardened state is too short, which may affect the workability and the construction quality of the grout, a retarder was added to the mixture in the pouring stage to guarantee favourable workability performance. As shown in Figure 3c, the initial and the final setting time increase significantly when the volumetric content of the S-series retarder increases from 0% to 0.15% and 0.2%. However, the M-series retarder with a volumetric content of 0.2% did not affect the setting time. The drawback of adding a retarder is that the early compressive strength of the UHPFRC may decrease. To make a compromise between the early concrete strength and setting time requirements of the grout, a volumetric content of 0.15% was finally selected for the S-series retarder. In most previous studies, the production of UHPFRC required high-temperature steam curing [39]. However, the new UHPFRC developed in this paper can be cured at room temperature and still exhibit excellent mechanical properties, as mentioned in authors' previous study [40]. Cylinders and cubes were prepared for each batch of grout, and these samples were demoulded after 24 hours and cured along with the column specimens until the test day.



(a) Slump flow test of the UHPFRC



(b) Grouting from a hole on top



(c) Setting time vs. slump flow curve under different retarder dosages

Figure 3. Workability of UHPFRC

2.1.2 Material properties

Tables 3 and 4 show the material properties of the UHPFRC and the steel tube, respectively, which were obtained through standard material tests. The experimental programme tested three $\Phi 100$ mm \times 200 mm concrete cylinders in accordance with ASTM C39/C39M-2014 [41], three 100 mm \times 100 mm \times 100 mm concrete cubes in accordance with GB/T 169 31387-2015 [42] and five concrete coupons in accordance with JSCE-2008 [43] after 28th day of curing to determine the material properties of the UHPFRC. The average compressive strength of the concrete cylinders reached 121 MPa, the average compressive strength of the concrete cubes reached 157 MPa, and the average tensile strength of the concrete coupons reached 7.9 MPa. All the steel tubes and plates were made of mild steel S355, and the shear keys were HRB 400 rebar. Tensile tests on the steel/rebar coupons, which were cut from different locations on both the inner and the outer tubes, were performed with a universal test machine in accordance with ASTM E8/E8M-2016 [44]. The Young's modulus E_s , yield strength f_y and ultimate strength f_u of the steel plate, steel tube and rebar are summarized in Table 4.

Table 3. Material properties of the concrete

Concrete	f_c (MPa)	f_{cu} (MPa)	f_t (MPa)	Poisson's ratio
UHPFRC-0.15%R	121	157	7.9	0.25

Notes: f_c =cylinder compressive strength; f_{cu} =cube compressive strength; f_t =coupon tensile strength.

Table 4. Material properties of the steel

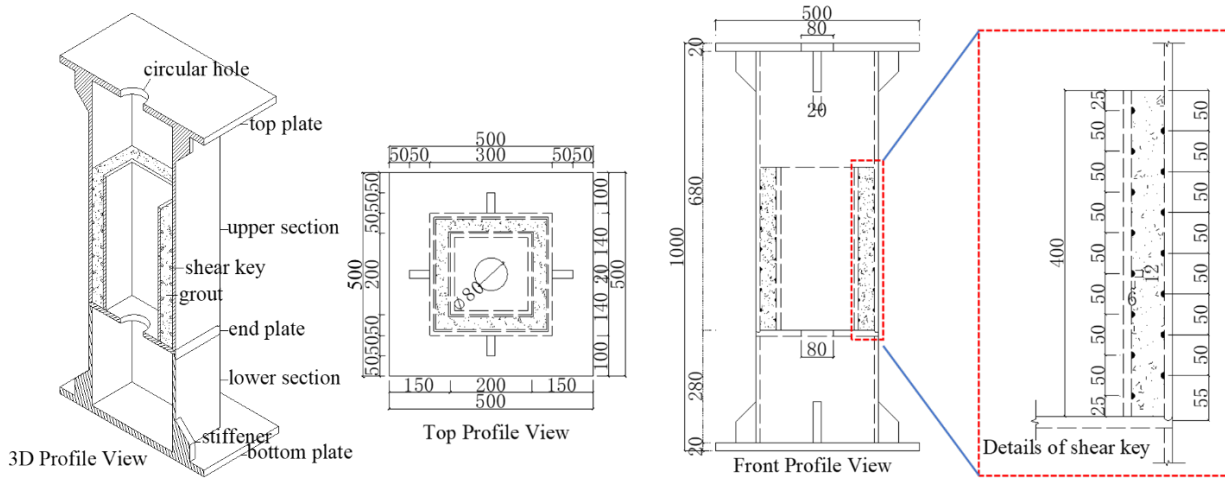
Item	Material	E_s (GPa)	f_y (MPa)	f_u (MPa)
Inner tube flat coupons	Mild steel	209	324	461
Inner tube corner coupons	Mild steel	211	517	588
Outer tube flat coupons	Mild steel	209	340	466
Outer tube corner coupons	Mild steel	211	511	587
Steel plate	Mild steel	209	352	478
Shear key	HRB 400 Φ 6	194	357	485

2.2 Test specimens

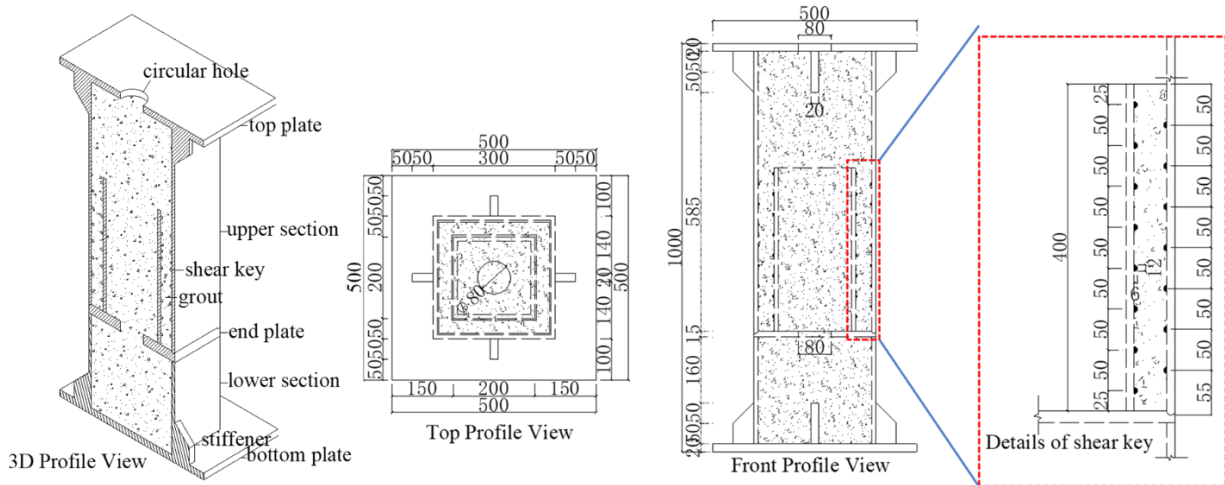
The experimental programme tested a total of eight full-scale SHS tubes that are classified into four types: (1) hollow steel tube, (2) fully grouted steel tube, (3) steel tube with a partially-grouted joint, and (4) steel tube with a fully-grouted joint. Two specimens were made for each of the above types for the axial compression and tension tests, respectively. The group 1 specimens serve as a reference to examine the

mechanical behaviour of the columns with grouted connections. Figure 4 shows the configuration and dimensions of the specimens with and without the UHPFRC grouted connections. Figures 4a and b show the partially-grouted and fully-grouted connected columns, respectively, whereas Figures 4c and d show the conventional steel tube and concrete-filled steel tube (CFST) composite column, respectively, which are used as references. The specimen with the grouted connection consists of an upper and a lower steel part. The lower part is fabricated by welding an inner tube onto a steel plate that is then welded to the top of the lower tube. The upper tube has the same size as the lower one and serves as an outer tube of the connection. Shear keys are welded to both the outside surface of the inner tube and the inside surface of the outer tube. The current research considers two grouting schemes to connect the upper tube to the lower one: (1) grouting only the space between the inner and the outer tube, which is referred to as the partially-grouted column, and (2) grouting the entire cavity of both the upper and the lower tubes, which is referred to as the fully-grouted column. The central holes of the top plates allow injection and flow of the UHPFRC grout and an overflow hole also locates at the end plate welded on the lower tube. Figure 4f shows the prefabricated steel tubes with sleeves.

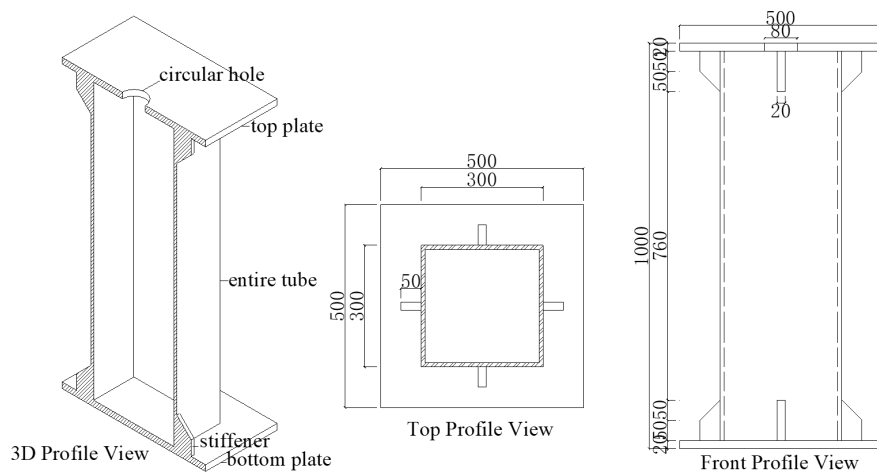
Table 5 presents the details of the test specimens, including the materials used, geometric parameters and loadings conditions. In this Table, NGEC indicates non-grouted entire column under compression; NGET indicates non-grouted entire column under tension; FGEC indicates fully-grouted entire column under compression; FGET indicates fully-grouted entire column under tension; PGCC indicates partially-grouted connected column under compression; PGCT indicates partially-grouted connected column under tension; FGCC indicates fully-grouted connected column under compression; and FGCT indicates fully-grouted connected column under tension. The specimens are designed with a nominal size of 300 mm(W)×300 mm(H)×8 mm(T), and the inner tube of the connection is designed with a nominal size of 200 mm×200 mm×8 mm. The shear keys are designed with a height of 6 mm and a width of 12 mm and are positioned with a spacing of 50 mm, as shown in Figures 4a and b.



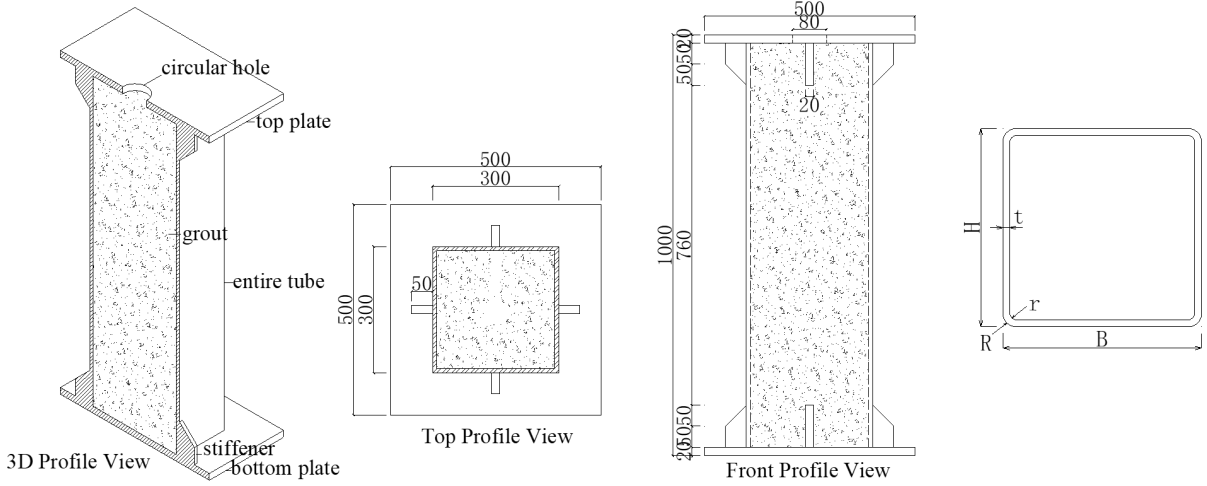
(a) PGCC/PGCT



(b) FGCC/FGCT



(c) NGEC/NGET



(d) FGEC/FGET

(e) Definition of symbols



(f) Prefabricated steel tubes with sleeves

Figure 4. Configuration and dimensions of the specimens

Table 5. Test matrix

Specimen (mm)	Tubular section	Width B (mm)	Height H (mm)	Thickness t (mm)	R (mm)	r (mm)	Grout type	Loading
NGEC	ET 300×300×8	301	301	7.80	20	10	No grout	Compression
NGET	ET 300×300×8	300	300	7.80	20	10	No grout	Tension
FGEC	ET 300×300×8	299	298	7.80	20	10	Fully grout	Compression
FGET	ET 300×300×8	300	300	7.80	20	10	Fully grout	Tension
PGCC	OT 300×300×8	298	302	7.80	20	10	Partially grout	Compression
	IT 200×200×8	202	201	7.75	15	8.5		
PGCT	OT 300×300×8	299	299	7.80	20	10	Partially grout	Tension
	IT 200×200×8	202	201	7.75	15	8.5		

FGCC	OT 300×300×8	299	301	7.80	20	10	Fully grout	Compression
	IT 200×200×8	202	202	7.75	15	8.5		
FGCT	OT 300×300×8	300	301	7.80	20	10	Fully grout	Tension
	IT 200×200×8	201	202	7.75	15	8.5		

Notes: ET=entire tube; OT=outer tube; IT=inner tube; B =width of the tube cross section; H =height of the tube cross section; t =tube thickness; R =fillet radius of the tube outer surface; r =fillet radius of the tube inner surface.

2.3 Test setup, loading procedure and measurement scheme

Figure 5 shows the setup of the tensile and compressive tests. A computer-controlled servo-hydraulic actuator with a tensile capacity of 5000 kN and a compressive capacity of 12,000 kN was used for the tests. For the tensile tests, the actuator was connected to the end plate with a ball joint connection mounted in the actuator to provide a uniform tensile force. The specimen was then connected to the end plate and bearing floor with high-strength bolts to transfer the tensile load to the specimens. For the compressive tests, the specimens were directly located on the bearing floor. The loads were applied under displacement control at a displacement rate of 0.2 mm/min. Figure 6 shows the measurement scheme for each type of specimen. Linear variable displacement transducers (LVDTs), T1, T2 and T3, were used to measure the lateral displacement along the height of the specimen, whereas T4 and T5 were placed vertically to measure the global axial displacement. Considering the symmetry of the SHS tubes, strain gauge pairs (S1-S12) aligned in both the axial and the circumferential directions were bonded on the outside surface of the specimens.

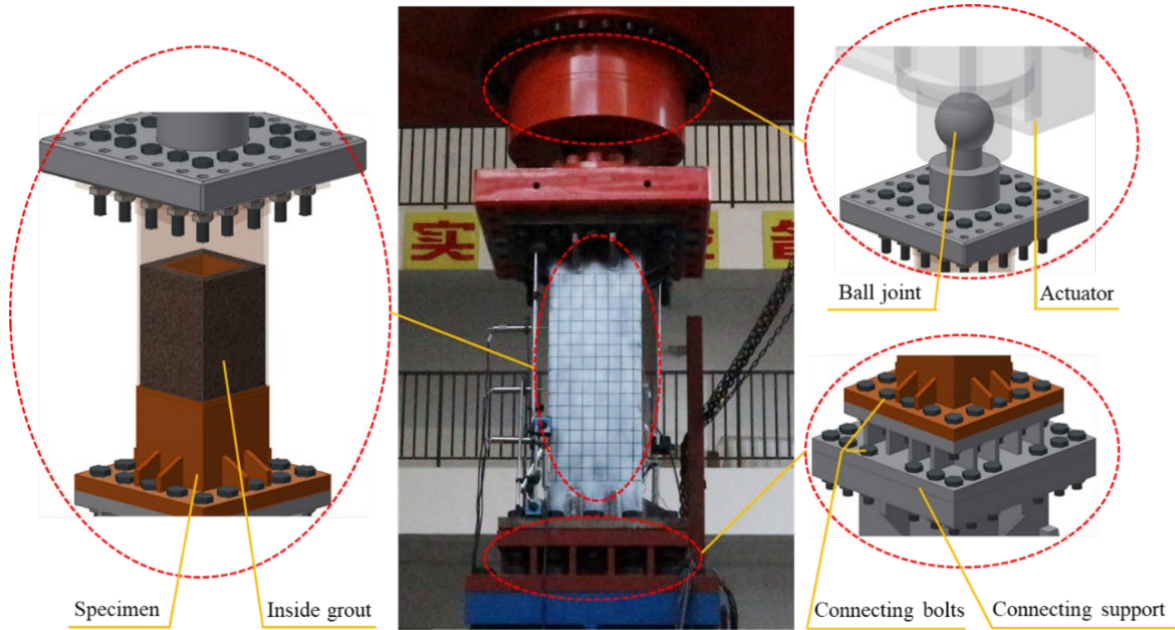


Figure 5. Test setup

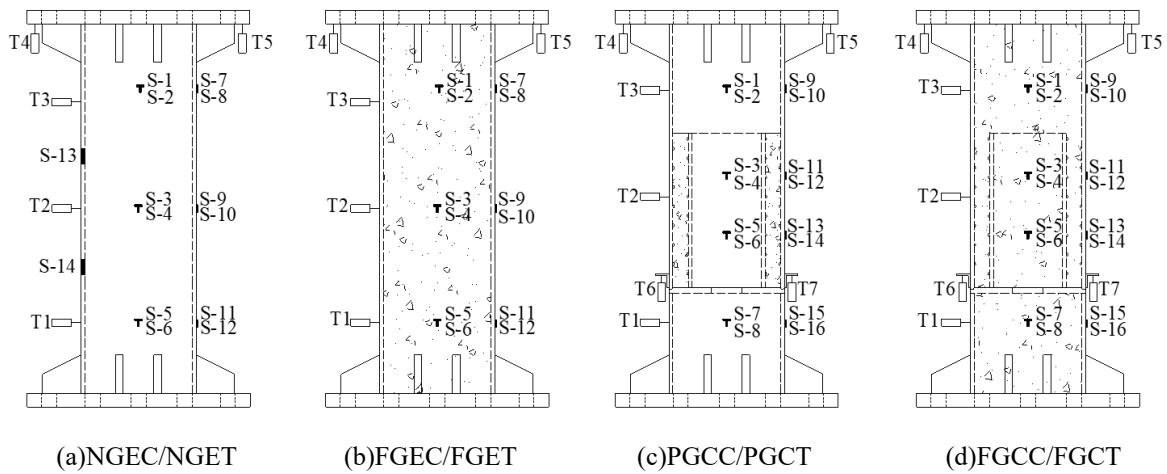


Figure 6. Measurement scheme

3. Test Results

3.1 Failure modes

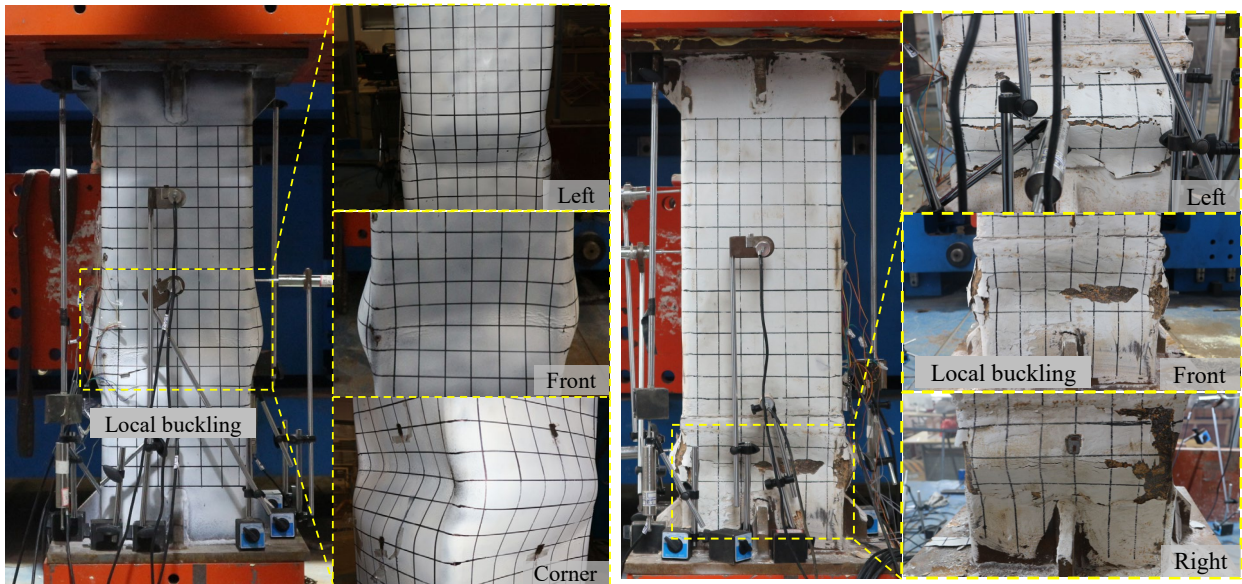
Figure 7 shows the three main failure modes observed in the grouted connections. For the compressive tests of specimens FGWC and FGCC, the tests were terminated when the load approached 75% of the machine capacity because the high compressive resistance might exceed the allowable loading capacity of the machine. Therefore, there was no obvious failure observed in these two specimens. For

specimens NGEC and PGCC, both failed due to buckling of the outer steel tube, as shown in Figures 7a and b. As expected, specimen NGEC was a conventional steel tube, and visible local buckling occurred in the mid-length of the steel tube. However, buckling of specimen PGCC initiated from a small deformation in the non-grouted region of the column. This phenomenon occurred because the sandwiched UHPFRC grout helped to improve the lateral stiffness of the steel tube. As the load increased, local buckling also occurred in the lower tube region, and the circumferential deformation increased rapidly, which demonstrated that the damage had bypassed the grouted connection; hence, the tube failed before failure of the connection. This observation shows that the strength of the grouted connection is greater than that of other parts, thus satisfying the seismic design principle of “strong joint-weak member”.

For the tensile tests, specimens NGET and FGET both failed because of the yielding of the outer tube, and obvious deformation occurred in these two specimens. However, specimen FGCT failed by punching shear of the steel end plate, as shown in Figure 7c. The punching surface was clearly seen after removing the lower tube section (Figure 15h). Similarly, specimen PGCT failed from weld tearing at the welding position between the inner tube and the end plate. During this failure, a sharp tearing noise emanated from the specimen, and a visible gap formed between the upper and lower tubes, as shown in Figure 7d. The steel end plate also had obvious bending deformation. The structural stiffness degraded significantly when approaching the failure load. Ultimately, the steel end plate and the weld were fully sheared off. The test results reveal that the end plate in the connected region is one of the most important and weakest parts in this grouted connection system. Therefore, enhancement in this region must be taken into consideration to prevent the end plate from unexpected failure. The failure also indicates that the UHPFRC grouted connection region has much higher shear strength than the inner tube. The high shear strength of the grouted connection verifies that it is feasible to use this novel grouted connection in prefabricated building structures. Figure 15f displays the internal picture of the UHPFRC grout after removing the outer tube. Based on the profile of the dent, very small slip can be observed between the shear keys and the grout.

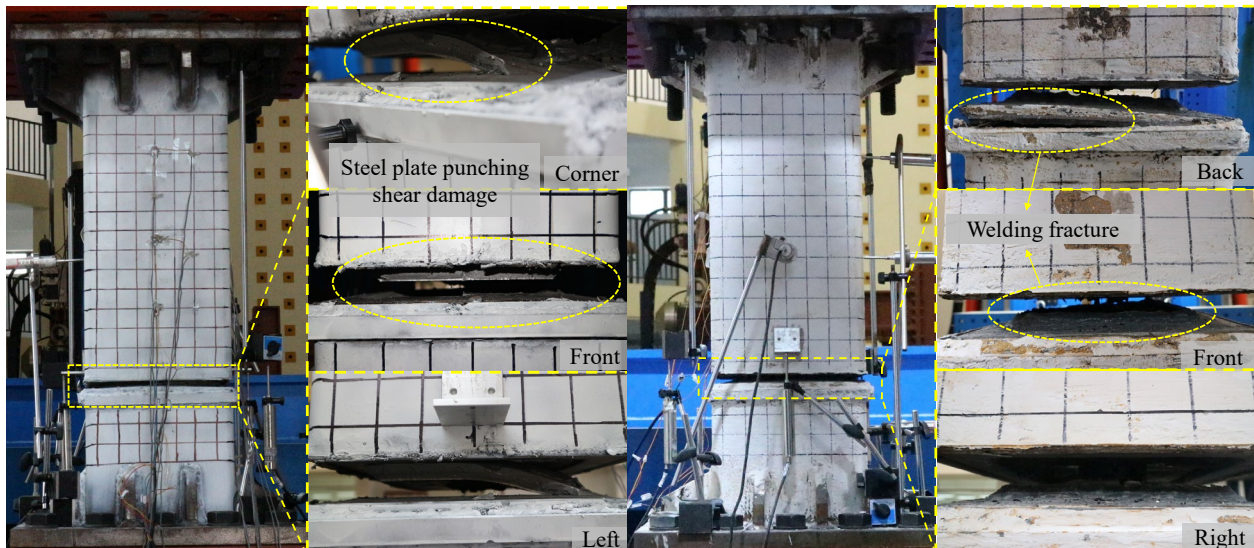
Figure 8 shows all the possible failure modes and corresponding load-displacement curves for the novel

UHPFRC grouted connection under tensile and compressive loads, i.e., (Mode A) grout shear damage, (Mode B) punching shear of the end plate or welding fracture, (Mode C) steel tube yielding, (Mode D) local buckling, and (Mode E) steel yielding and concrete crushing. The analysis of failure modes can provide an insight understanding of the load transfer mechanism in the novel grouted connection. Moreover, the analysis also serves as a guidance for further design of the UHPFRC connections in prefabricated columns.



(a) NGEC-local buckling

(b) PGCC-local buckling



(c) FGCT-punching shear damage

(d) PGCT-welding fracture

Figure 7. Failure modes

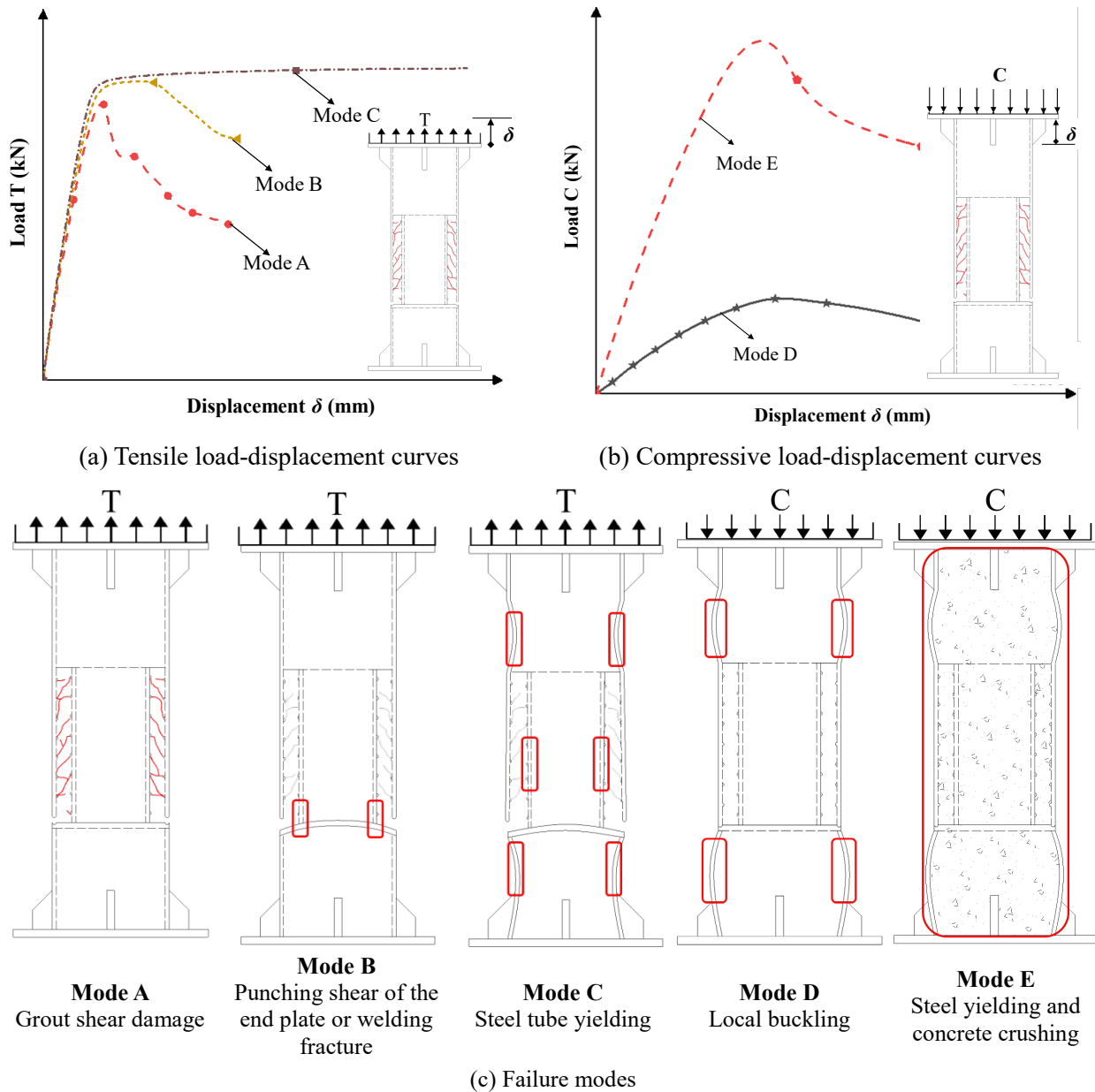


Figure 8. Possible failure modes and corresponding load-displacement curves of the grouted connections

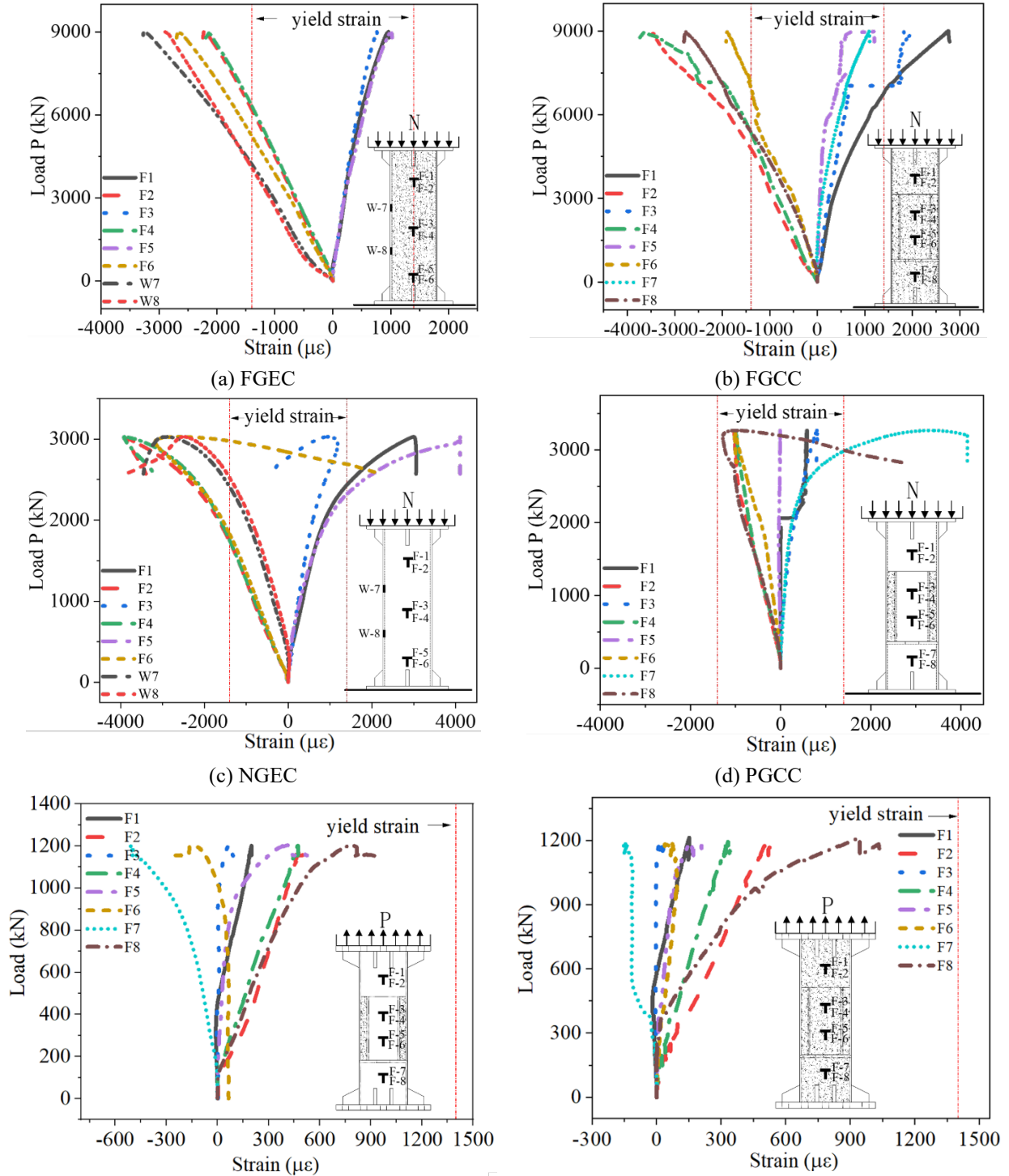
3.2 Load-strain relationship

Figure 9 shows the load-strain curve of each specimen. Under axial compression, the ultimate load of specimens FGCC and FGEC is approximately 9000 kN because the test terminates due to the limited machine capacity. Specimen FGEC begins to yield at approximately 4100 kN, whereas yielding of specimen FGCC starts at approximately 4800 kN, which shows that a column with a grouted connection

has a higher compressive stiffness, as shown in Figures 9a and 9b. For specimens NGEC and PGCC, the ultimate compressive resistance is approximately 3000 kN because both fail due to local buckling of the steel tube. The compressive resistance of specimen PGCC is slightly larger than that of specimen NGEC due to the shorter buckling lengths. In contrast to specimen NGEC (see F3 and F4), the stress of the grouted region (see F4 and F6) of specimen PGCC is far from the yielding point. This grouted connection exhibits either a comparable compression resistance with or even higher compression resistance than that of the column without grouted connection. Under tension, specimens FGWT and NGET both begin to yield when the load reaches approximately 2500 kN. No obvious failure pattern appears until the steel tube completely yields. However, specimens PGCT and FGCT do not reach the yielding stage because they suffer from early punching shear damage of the steel end plate and weld tearing damage between the end plate and the inner tube. This finding indicates that the shear strength of the UHPFRC grouted region is higher than the punching shear strength of the end plate. The punching shear failure of the end plate is attributed to the high strength of the UHPFRC.

The distribution of the longitudinal and circumferential strain along the specimens are shown in Figures 10a-d. The specimen is divided into the upper tube, the grouted connection region and the lower tube. For the compressive specimen PGCC, the longitudinal strain develops rapidly, and the steel tube yields outside the grouted region. However, the strain in the grouted region is far below the yield strain due to the constraint effect of the UHPFRC grout, implying that the axial load is well transferred from the upper tube to the lower tube through the UHPFRC grouted connection. A large circumferential strain is achieved since a visible buckling deformation occurs in the lower tube. For the tensile specimen PGCT, the longitudinal strain in the grouted region is also far smaller than that in the other regions. When the tensile load increases, neither longitudinal strain nor circumferential strain reaches the yield strain of the steel due to the early fracture of the weld. The maximum longitudinal strain along the specimen is less than 800 microstrain. The upper tube region expands while the lower tube region shrinks, leading to tensile strains in the circumferential direction of the upper tube and compressive strains in the lower tube. This phenomenon occurs due to the punching shear deformation of the steel end plate, which further induces inward concave deformation of the lower tube. Nevertheless, to induce grout failure and prevent punching shear failure of

the end plate, further studies should focus on reducing the strength of the sandwiched grout and strengthening the end plate. Therefore, from the compressive and tensile tests on the novel grouted connection, it should be noted that the connection exhibits acceptable compressive and tensile performance, which is effective in transferring the force from the upper column to the lower column.



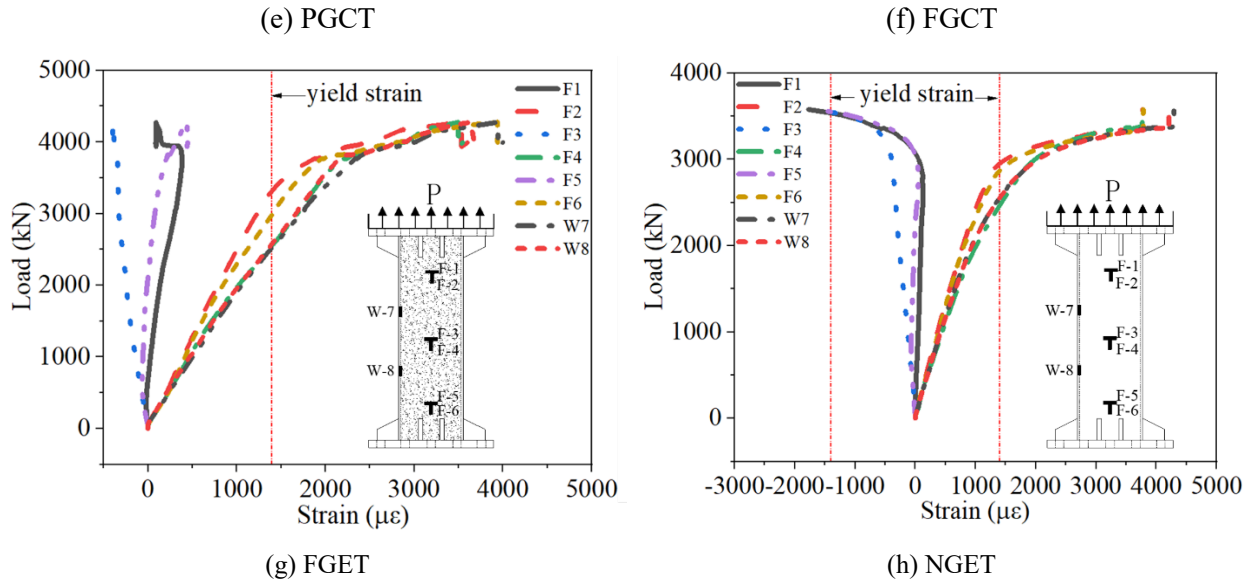


Figure 9. Load-strain curves

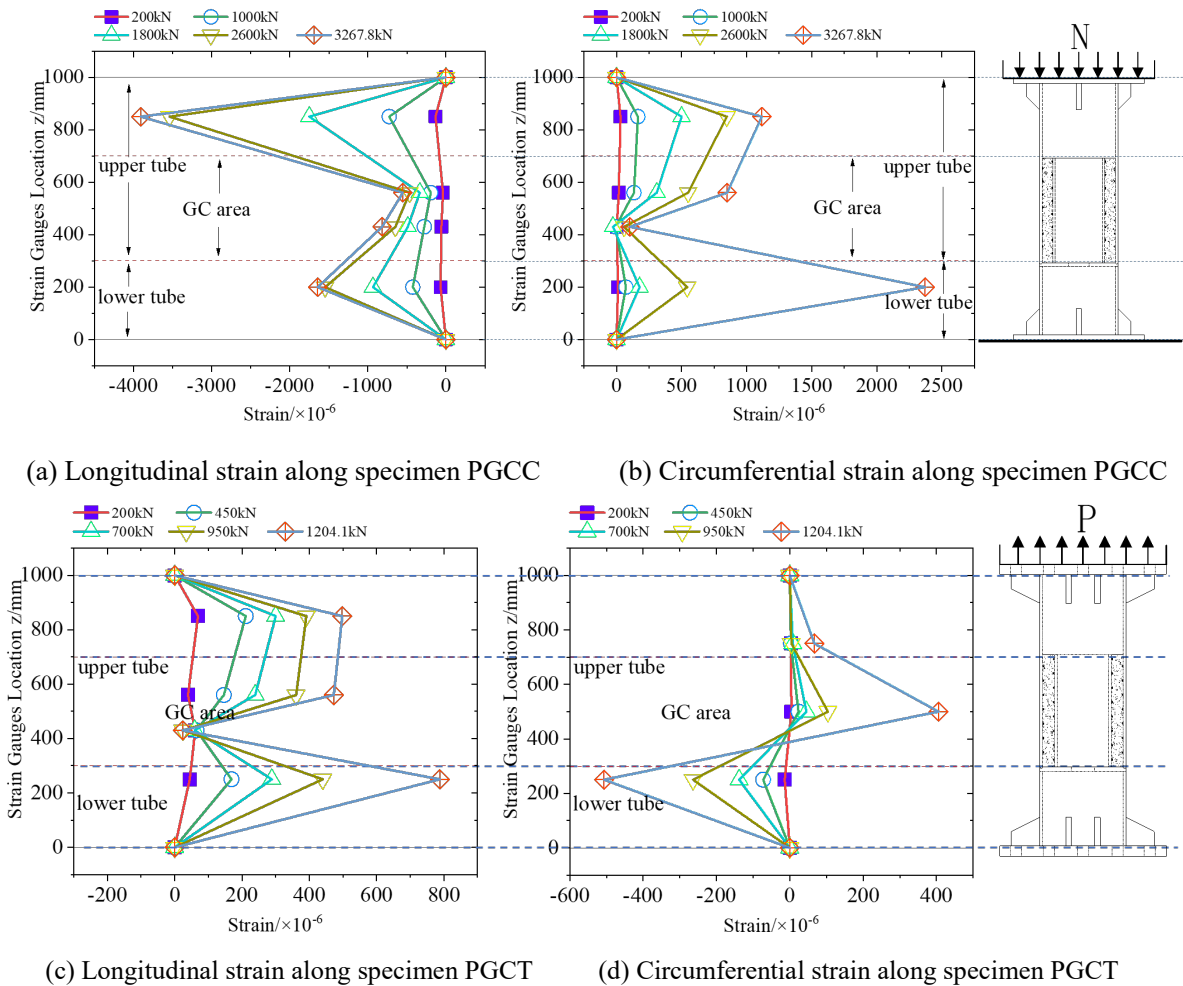


Figure 10. Strain distribution in the specimens

4. Finite Element Analysis

To capture a more detailed failure mechanism of the connections during the loading history and build confidence for future parametric analysis, the current study conducts advanced FE analysis on each specimen using ABAQUS. This section presents the details of the material models of the UHPFRC and the steel, the element type, meshing scheme and the contact definition for the steel and concrete. The FE results are then verified against the test results.

4.1 Material model of the concrete

The FE analysis adopts the concrete damaged plasticity (CDP) model [45, 46] to represent the behaviour of the UHPFRC. The CDP model can accurately simulate the macroscopic response of concrete material. Moreover, this model also considers the compression "softening phenomenon" when subjected to tension in 2-dimensional or 3-dimensional state of stress, which allows the mechanical behaviour of concrete to be accurately simulated. The parameters for the CDP model are the modulus of elasticity (E_0), Poisson's ratio (ν), dilation angle (w), second stress invariant ratio (K_c), ratio of biaxial to uniaxial compressive strength (r_{b0}/r_{c0}), parameter of the flow potential $G(\varepsilon)$, and viscosity factor. In this model, the values of all the parameters and modelling techniques are based on the previous studies of UHPFRC [47, 48] and are calibrated with the test results. The values for w , K_c , r_{b0}/r_{c0} , $G(\varepsilon)$ and the viscosity factor are finally set to be 54° , 0.667, 1.07, 0.1 and 0.0001, respectively [47].

The compressive stress-strain relations presented in GB 50010-2010 [49] are used for the FE analysis to simulate the UHPFRC. A nonlinear equation in dimensionless form is given in Eq. (1), and the stress-strain curve is shown in Figure 11.

$$y = \begin{cases} \frac{Ax}{1+(A-1)x^{\frac{A}{A-1}}} & 0 \leq x \leq 1 \\ \frac{x}{B(x-1)^2+x} & x > 1 \end{cases} \quad (1)$$

where $B = 2.41$ is the descending parameter and $A = E_0 \varepsilon_{pc} / f_c$ is the ascending parameter, in which $E_0 = \sigma_{c0}^{e0} / \varepsilon_{c0}^{e0}$ is the elastic modulus ($\sigma_{c0}^{e0} = 1/2 f_c$ is the elastic limit point stress), f_c is the compressive peak stress and ε_{pc} is the corresponding strain [50].

For normal concrete, cracks occur when the strain exceeds the tensile strain. The uniaxial tensile stress-strain relation of normal concrete is assumed to be linear until the ultimate tensile strength f_t is reached. However, for the UHPFRC, the embedded steel fibres provide a bridging effect that prevents crack propagation, resulting in multi-cracking and strain hardening after the first crack [51, 52, 53]. To make the tensile stress-strain relationship applicable to the nonlinear analysis, Uchida et al. [39] simplified the tensile stress-strain relationship and proposed a trilinear model, as shown in Figure 11. When the first crack occurs, the corresponding stress is defined as the peak stress f_t . After this point, the stress magnitude remains the same in a strain hardening state, which is followed by a softening phase, wherein the stress decreases.

Among the input data of tensile properties in the CDP model, f_t is the peak strength obtained from the direct tensile test of the concrete coupon, the elastic modulus E_{0t} is defined as equal to E_{0c} , the cracking strains ε_1 and ε_2 can be calculated by $\varepsilon_1 = \omega_1 / L_{eq}$ and $\varepsilon_2 = \omega_2 / L_{eq}$, ω_1 and ω_2 are the crack opening displacements obtained from the tensile test, and L_{eq} is the unit characteristic length, which is related to the selected element type and element size in the FE model [54].

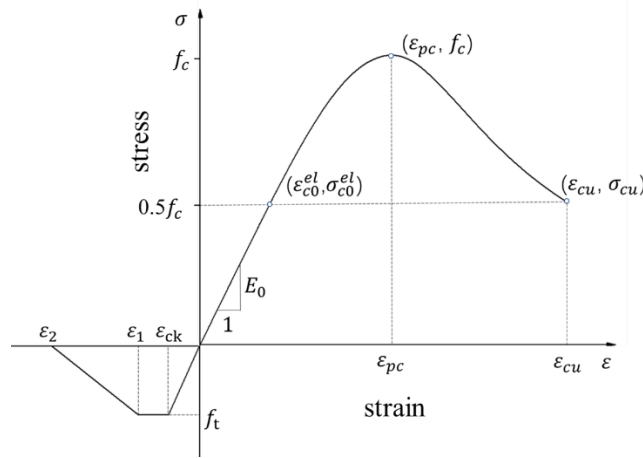


Figure 11. Constitutive model of concrete for FE analysis

The compressive and tensile damage variables are defined as follows:

$$d_c = 1 - \frac{\sigma_c E_0^{-1}}{\varepsilon_c^{pl} \left(\frac{1}{b_c} - 1 \right) + \sigma_c E_0^{-1}} \quad (2)$$

$$d_t = 1 - \frac{\sigma_t E_0^{-1}}{\varepsilon_t^{pl} \left(\frac{1}{b_t} - 1 \right) + \sigma_t E_0^{-1}} \quad (3)$$

where $b_c = \varepsilon_c^{pl} / \varepsilon_c^{in}$ and $b_t = \varepsilon_t^{pl} / \varepsilon_t^{ck}$ are the constant factors obtained from Birtel and Mark [55], which are 0.7 and 0.1, respectively; ε_c^{in} and ε_t^{ck} are the compressive and tensile inelastic strains, which are calculated by $\varepsilon_c^{in} = \varepsilon_c - \sigma_c / E_0$ and $\varepsilon_t^{ck} = \varepsilon_t - \sigma_t / E_0$; and ε_c^{pl} and ε_t^{pl} are the plastic strain for concrete in compression and tension, respectively, which are calculated automatically by the software using the values of ε_c^{in} and ε_t^{ck} . The values of ε_c^{pl} and ε_t^{pl} are neglected, as recommended by Chi et al. [56]. Figure 12a shows the relation between the compressive strength and damage variable d_c versus inelastic strain, and Figure 12b shows the relation between the tensile strength and damage variable d_t versus inelastic strain in the FE analysis.

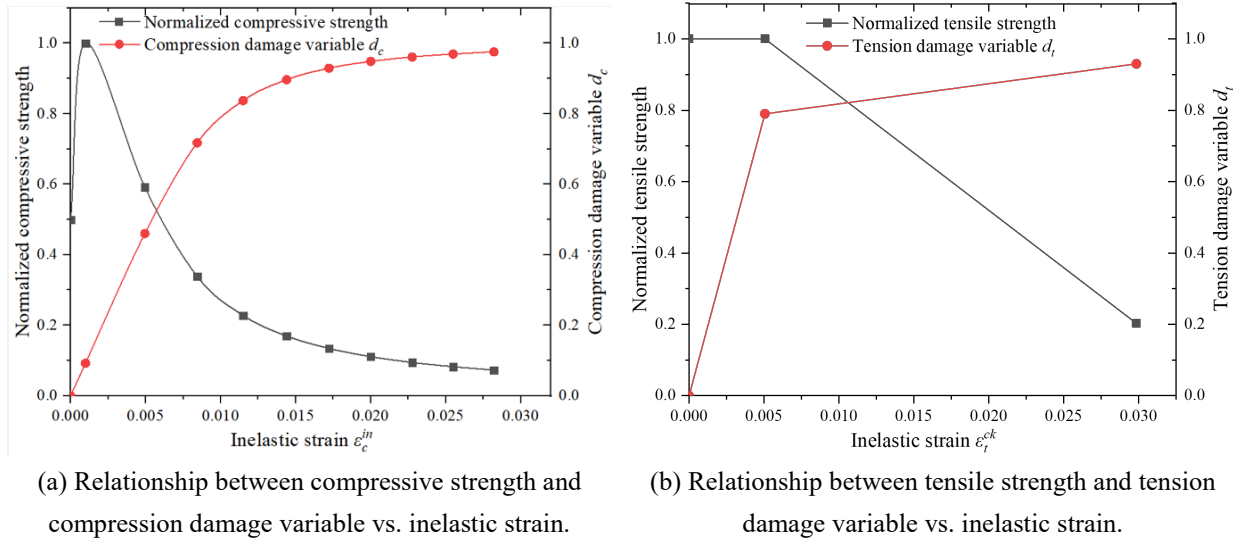
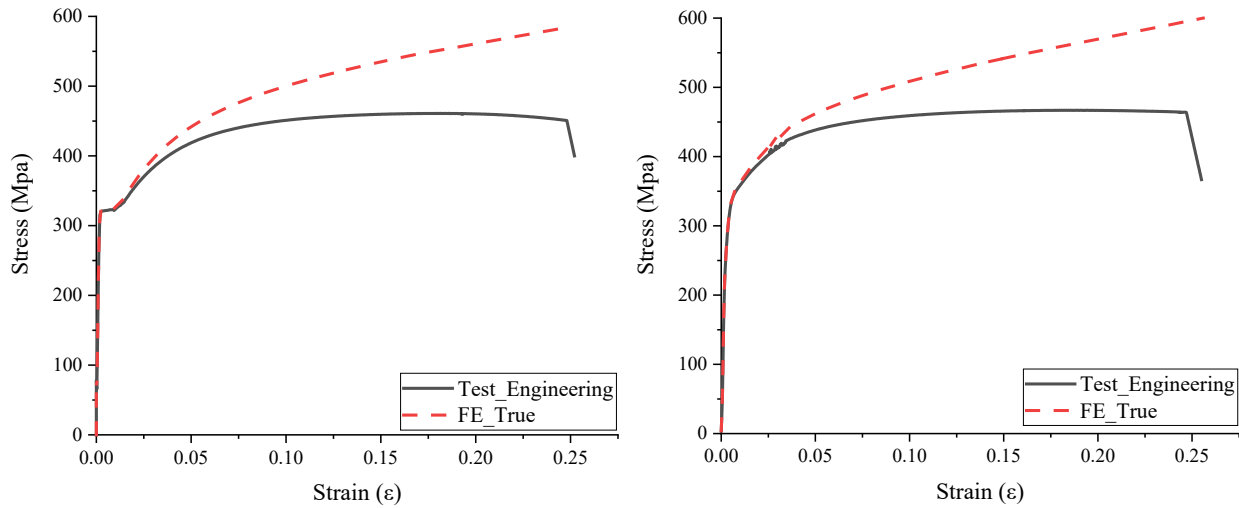


Figure 12. CDP model

4.2 Material model for the steel

The material model for the SHS tubes, steel plates, and shear keys is the elastic-plastic model. The engineering stress-strain curves are obtained from the tensile tests of the steel coupons, whereas in the FE model, the engineering stress-strain relations are converted to true stress-strain relationships and used as input data, as shown in Figures 13a and 13b. Since the round corner of the SHS tube hardens in the cold-forming process during fabrication, the material properties of this part are defined separately.



(a) Stress-strain curves of the inner tube (flat coupons) (b) Stress-strain curves of the outer tube (flat coupons)
 Figure 13. Comparison of engineering stress-strain curves and true stress-strain curves

4.3 Element types and meshing scheme

In the FE model, all the material parts are well partitioned to achieve a regular hexagonal structural element shape to improve numerical convergence. Eight-node solid elements with reduced integration (C3D8R) are used to model the grout and steel. In the thickness direction of all material, a minimum of three elements are used. For the region outside the grouted connection, a coarse mesh with an element size of 10 mm is used, whereas for the grouted region, an 8 mm mesh is used. The total number of elements is 129680. Figure 14 shows a quarter of the FE model of the column with the novel grouted connection under a tensile load. Both ends of the column are fixed. However, in the nonlinear local buckling analysis, the steel tube is subjected to a large bending moment. To improve the simulation efficiency, the incompatible mode eight-node solid elements (C3D8I) are used to model the steel tube, which overcomes the shear locking problem and provides higher calculation accuracy.

4.4 Contact definition

Surface-to-surface contacts are used to simulate the interfacial interaction between the steel tubes and the UHPFRC grout. The surface of the stiffer body is normally selected as the master surface. However, since the lateral stiffness of the infilled grout is much higher than that of the steel tube, although the elastic modulus of the steel is much higher than that of the concrete, the inner surface of the outer tube and the

outer surface of the inner tube are set as slave surfaces, whereas the outer surface of the UHPFRC grout is set as a master surface. For the contact properties, hard contact is assumed in the normal direction, and an isotropic penalty friction with a constant friction coefficient of 0.7 [28] is utilized to represent the tangential friction between the steel and the UHPFRC grout.

4.5 Comparison of the FE results and test results

The test results presented in Section 2 are used to validate the developed FE model. Figure 12 shows a quarter model of the SHS column with grouted connections. The UHPFRC grout, the upper and lower tubes, and the shear keys are modelled independently. Both ends of the column are welded to the end plates and stiffened to ensure that failure will not occur at the column ends. The corresponding boundary conditions are applied at the planes of symmetry.

Figures 15a-15h show the failure modes of the columns under tensile forces observed from the tests and predicted by the FE simulations. From the figures, the FE simulations can accurately predict the failure patterns of the columns. For the compression tests on the steel column without grouting (i.e., specimen NGEC) and the column with the grouted connection (i.e., specimen PGCC), the FE simulation reproduces the local buckling of the steel tubes. For the tensile tests on the columns with grouted connections (i.e., specimens PGCT and FGCT), the punching shear failure of the end plate and the welding fracture are also predicted successfully in the FE simulations. Figures 16a-16h also compare the load-displacement curves of the specimens. The load-displacement curves obtained from the FE analysis accurately match the ones from the tests. The high strength of the UHPFRC guarantees the integrity of the infilled grout, and the nonlinear behaviour of the column connection or column is mainly governed by the steel tubes. The geometric and material parameters of the steel tube, such as the diameter, thickness, and yield strength, significantly affect the failure mode and ultimate resistance of the column with a grouted connection. Future research will be performed to quantify the effects of these parameters.

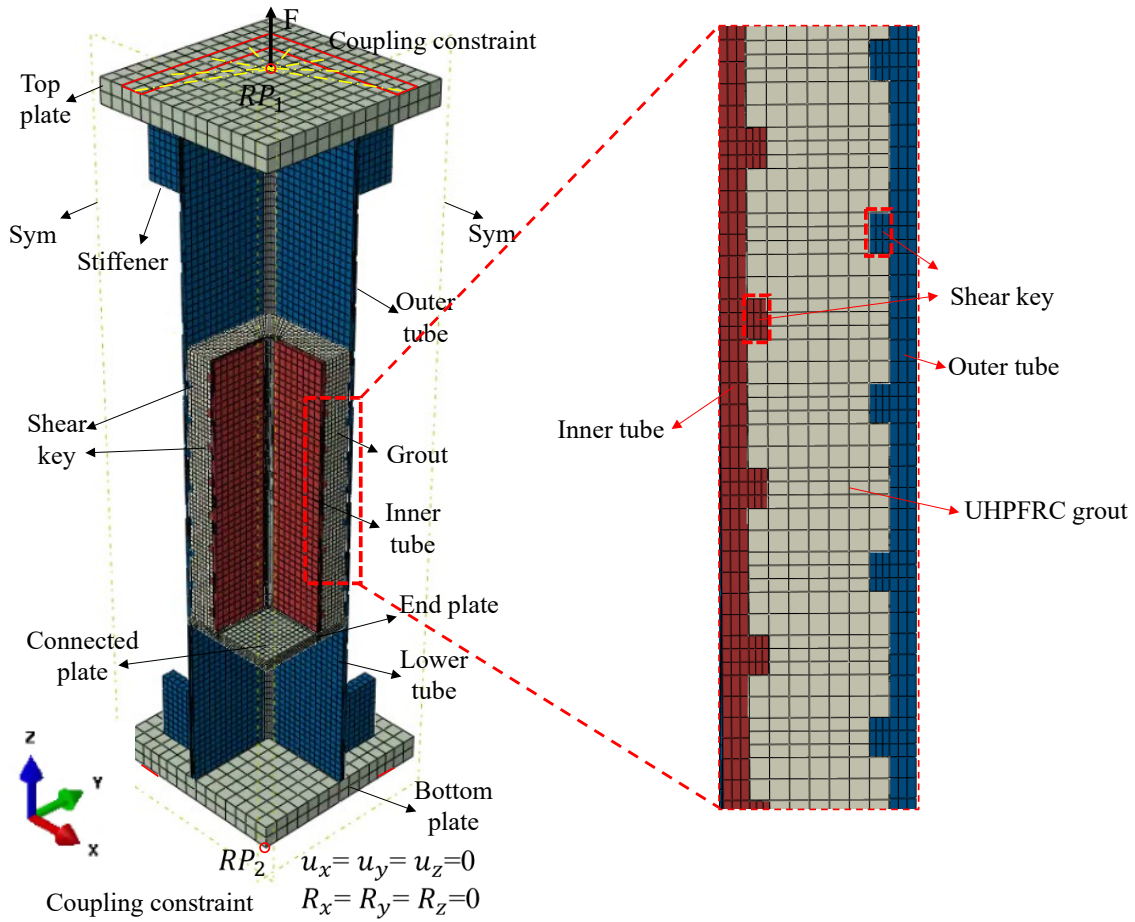
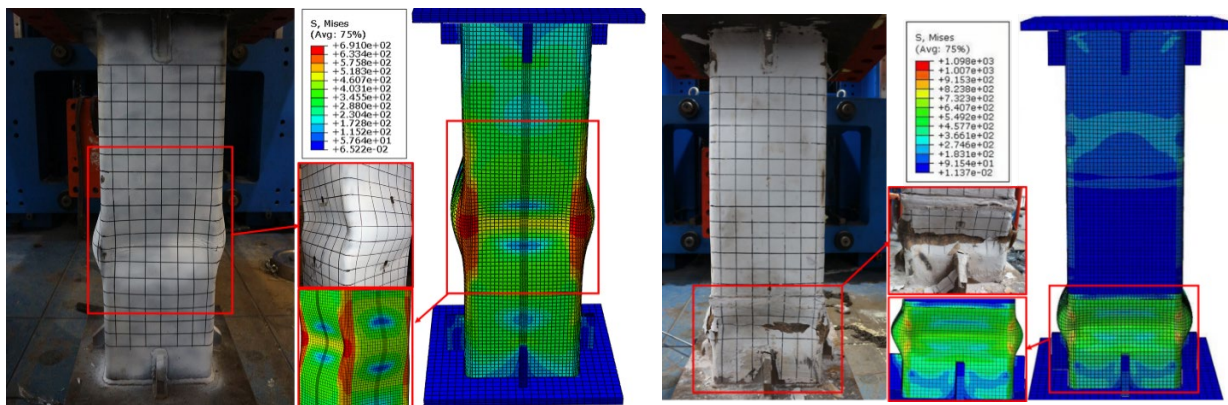
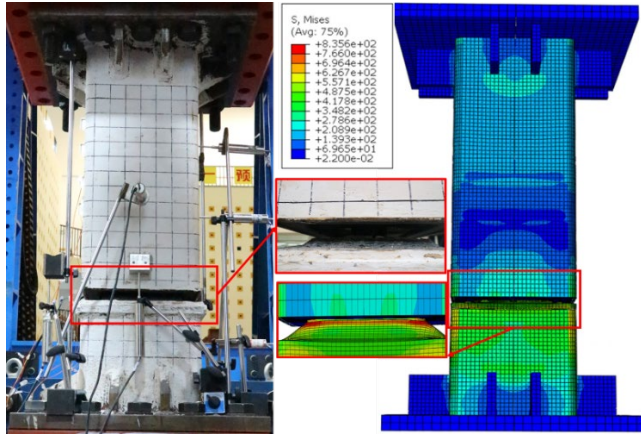


Figure 14. Quarter FE model of the grouted connection under a tensile force

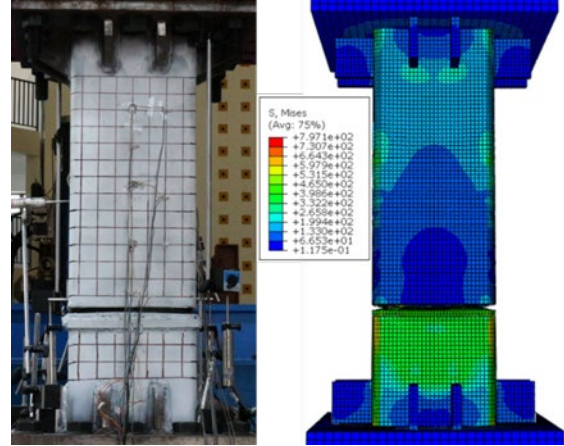


(a) NGEC-local buckling

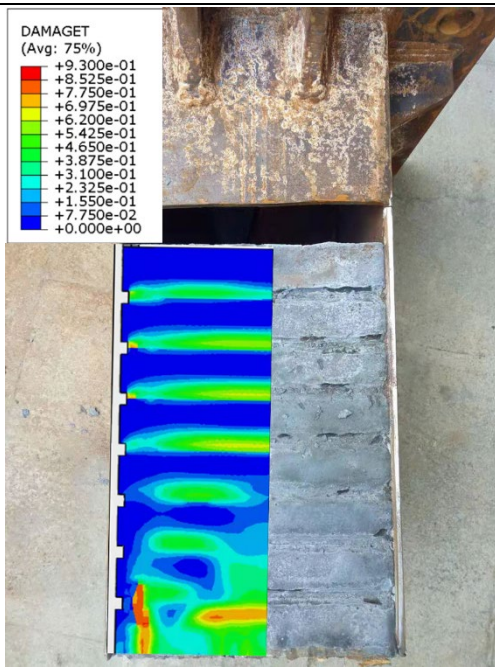
(b) PGCC-local buckling



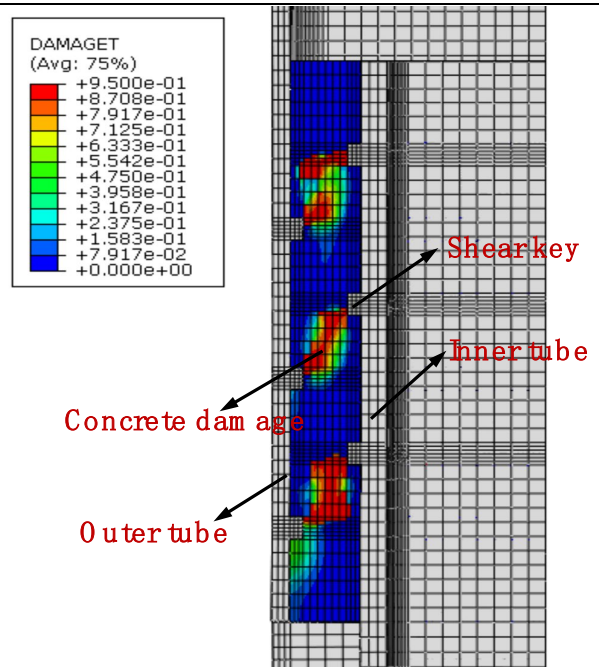
(c) PGCT-welding fracture



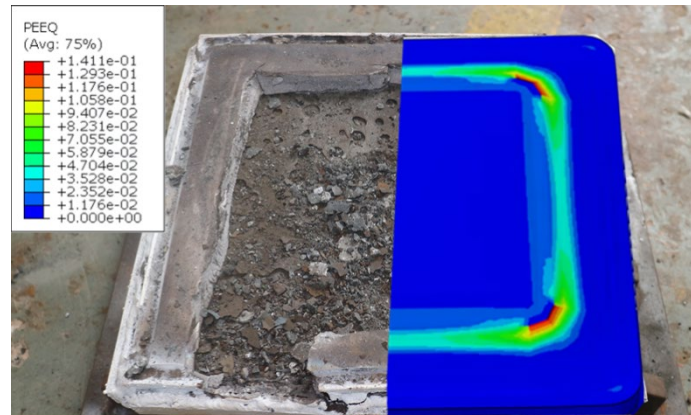
(d) FGCT-punching shear failure



(f) PGCT-grout damage

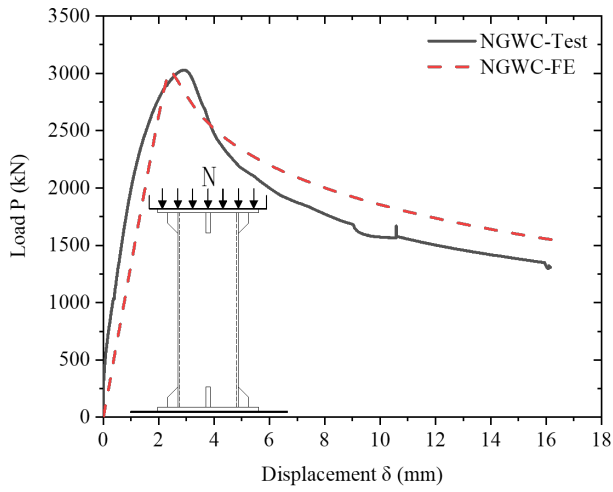


(g) Concrete shear failure

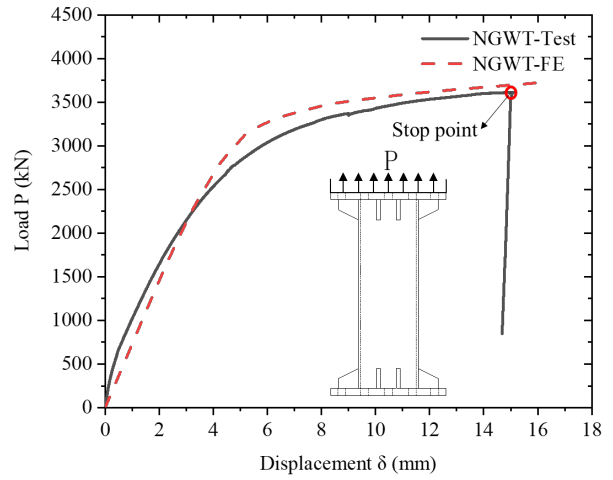


(h) FGCT-punching shear failure of the end plate

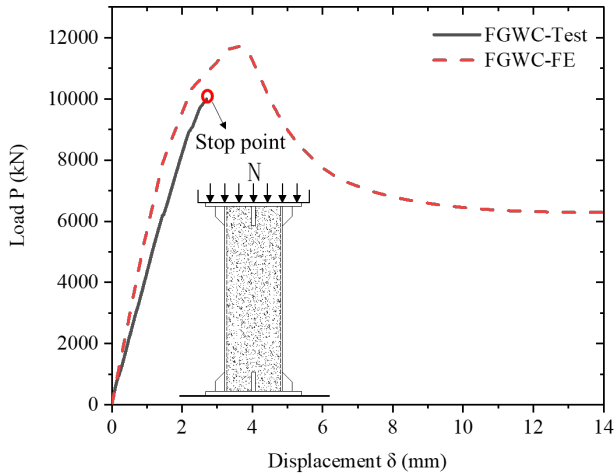
Figure 15. Comparison of failure modes between the FE and test results



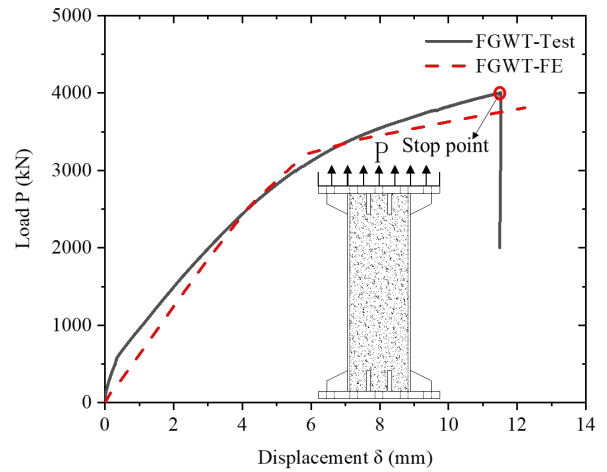
(a) NGEC



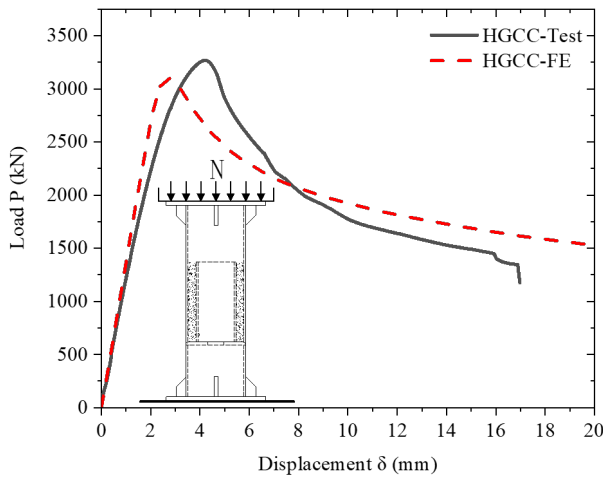
(b) NGET



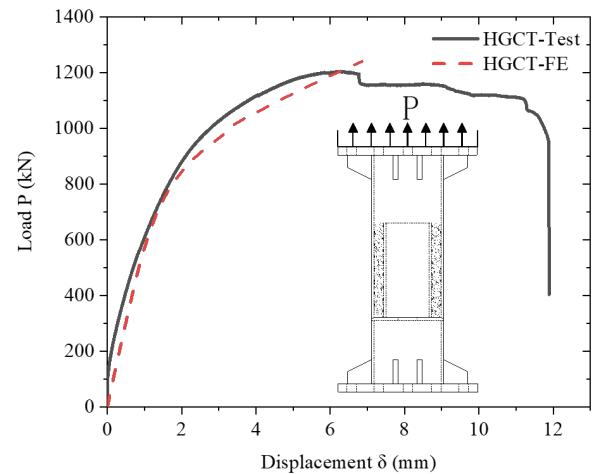
(c) FGEC



(d) FGET



(e) PGCC



(f) PGCT

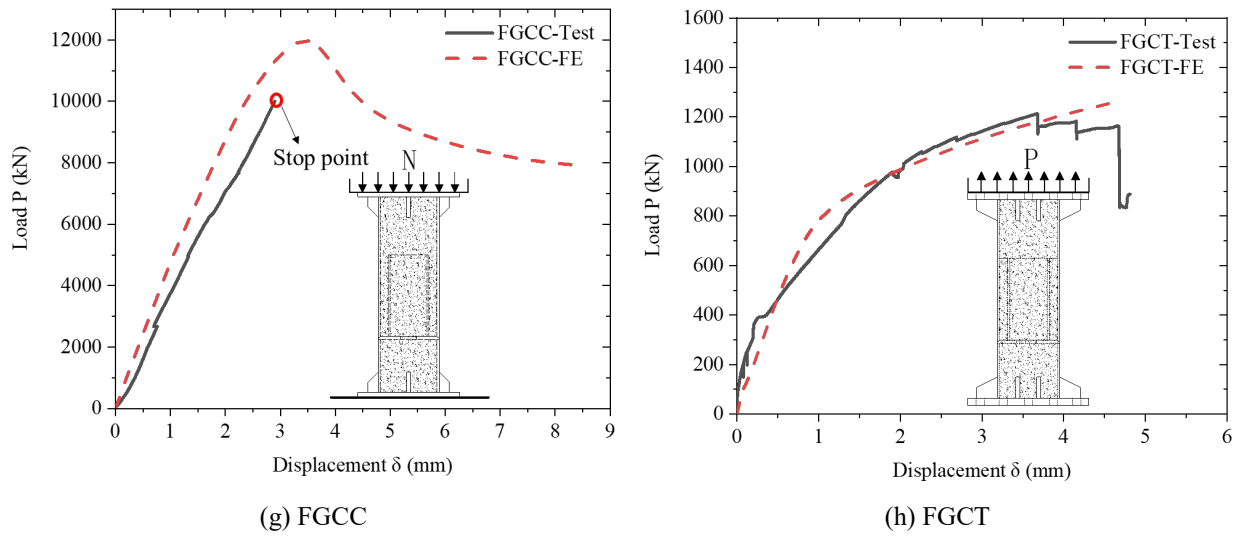


Figure 16. Comparison of the load-displacement curves between the test and FE results

5. Analysis on Ultimate Resistance and Verification

5.1 Analytical model

Based on the test observations, the primary failure modes of the unwelded, unbolted, grouted connection are buckling of the steel tube, punching shear failure of the end plate, welding fracture and yielding of the steel tube. Thus, the corresponding ultimate resistance of the grouted connections is governed by each failure mode. To guide the design of the new grouted connection, this section evaluates the existing analytical models using the test results obtained in this study.

5.1.1 Buckling of the steel tube

For the specimens under compression, specimens NGEC and PGCC exhibit local buckling failure of steel tube, as illustrated in Figure 7. Eurocode 3 [57] provides a formula to evaluate the compressive resistance of a steel tube with a local buckling failure pattern, which is given in Eq. (4).

$$N_b = \chi f_{ya} A_g \quad (4)$$

$$f_{ya} = f_{yb} + (C n t^2 / A_g) \times (f_u - f_{yb}) \quad (5)$$

where N_b is the buckling resistance of the member under compression; f_{ya} is the yield strength of steel, which takes into account the influence of cold forming; χ is the reduction factor for the relevant buckling

mode; f_{yb} and f_u are the characteristic tensile yield strength and tensile ultimate strength of the steel (MPa), respectively; t is the steel thickness before cold forming (mm); A_g is the gross cross-sectional area (mm²); C is a coefficient that is a function of the type of forming, e.g., $C = 7$ for a rolled material and $C = 5$ for other forming methods; and n is the number of 90° bends in the section with an internal radius less than $5t$.

5.1.2 Punching shear of the steel plate

The end plates are subjected to complex forces, which causes punching shear failure. Figure 17 shows a simplified model of the punching shear of the steel end plate. Packer and Henderson [58] described this failure mechanism using Eq. (6).

$$N_1 \sin \theta_1 = \frac{f_{y0}}{\sqrt{3}} t_0 \cdot 4b_{e,p} \quad (6)$$

$$b_{e,p} = \left(\frac{10}{b_0 / t_0} \right) b_1 \quad \text{but } \leq b_1 \quad (7)$$

where N_1 is the ultimate axial load, f_{y0} is the yield strength of the steel plate (N/mm²), θ_1 is the angle between the plate and the inner tube (herein, $\theta_1 = 90^\circ$), t_0 is the plate thickness (mm), $b_{e,p}$ is the effective punching shear width (mm), b_0 is the external width of the plate (mm), and b_1 is the external width of the inner tube (mm).

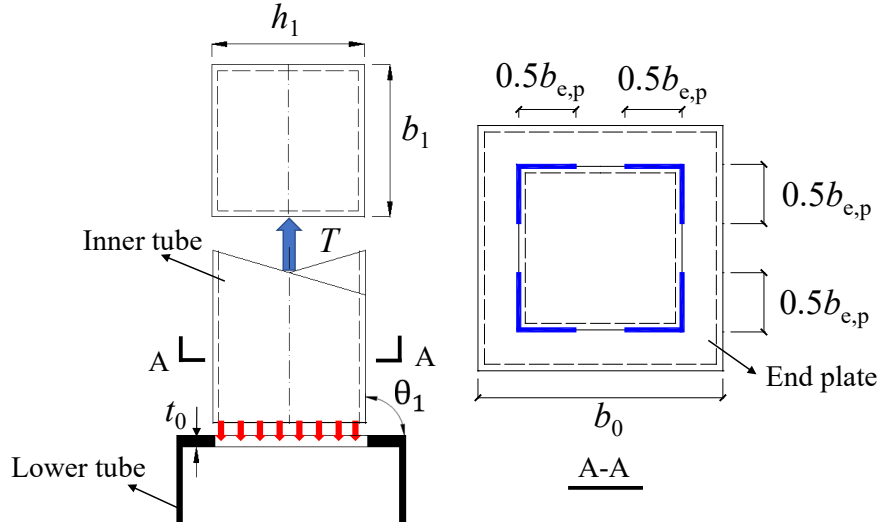


Figure 17. Simplified model of punching shear in the end plate

5.1.3 Welding fracture

Welding fracture, as a possible failure mode of the grouted connection system, occurs due to the initial imperfection in the weld between the inner tube and end plate. Eq. (8) is the formula for the ultimate tensile strength of the weld.

$$N = \sigma_f l_f h_e \quad (8)$$

where N is the ultimate axial load; σ_f is the yield strength of weld (MPa); l_f is the weld length, which is given by $l_f = l - 2h_f$ (mm); h_e is the effective thickness of the fillet weld, which is given by $h_e = 0.7h_f$ (mm); and h_f is the fillet weld height (mm).

5.1.4 Yielding of the steel tube

For specimens NGET and FGET, there is no obvious failure pattern but steel tube yielding occurs. The measured tensile load when the corresponding longitudinal strain reaches $5000 \mu\epsilon$ is defined as the tensile strength for specimens NGET and FGET [16]. The tensile strength of the hollow steel tube and CFST column are expressed in Eqs. (9) and (10), respectively.

$$N_{tu-h} = f_y A_s \quad (9)$$

$$N_{tu-CFST} = (1.1 - 0.4\alpha) f_y A_s \quad (10)$$

where N_{tu-h} and $N_{tu-CFST}$ are the axial tensile resistance of the hollow steel tube and CFST columns, respectively; f_y is the yield strength of steel tube (N/mm^2); A_s is the cross-sectional area of the steel tube (mm^2); and α is the steel contribution ratio, which is given by $\alpha = A_s / A_c$.

For specimens FGEC and FGCC, the tests are terminated because of their high compressive resistance, which exceeds the allowable machine capacity. The plastic compressive resistance of these two CFST composite columns can be calculated from Eqs. (11)-(13) according to Eurocode 4 [59].

$$N_{pl} = \eta_a A_a f_y + A_c f_c \left(1 + \eta_c \frac{t}{d} \frac{f_y}{f_{ck}}\right) \quad (11)$$

$$\eta_a = 0.25(3 + 2\bar{\lambda}) \quad (12)$$

$$\eta_c = 4.9 - 18.5\bar{\lambda} + 17\bar{\lambda}^2 \quad (13)$$

Where, N_{pl} is the plastic resistance; A_a is the cross-sectional area of the structural steel (mm^2); f_y is the yield strength of the structural steel (MPa); A_c is the cross-sectional area of the concrete (mm^2); f_{ck} is the characteristic compressive strength of the concrete cylinder (N/mm^2); t is the steel tube thickness (mm); d is the width of the steel section (mm), and $\bar{\lambda}$ is the relative slenderness ($\bar{\lambda} = \sqrt{N_{pl,Rk} / N_{cr}}$).

5.2 Verification

Table 6 presents the maximum loads from the tests, FE analyses and the predictions using the above equations. From the table, it is shown that the average values of P_{pre}/P_{test} and P_{FE}/P_{test} are 1.06 and 1.01, respectively, with standard deviations of 0.05 and 0.03. The existing failure-based models can provide close predictions of the maximum load with small standard deviations for all the specimens in terms of different failure modes. Figure 18 plots the predictions against the results from the tests and FE simulations, which shows a good accuracy of the existing analytical formulas. The comparisons again demonstrate that the existing analytical formulas can potentially be used in the design of prefabricated columns with UHPFRC grouted connections.

Table 6. Comparison of test, FE and predictive maximum loads and failure modes

Specimen	P_{test}	P_{pre}	P_{FE}	P_{pre}/P_{test}	P_{FE}/P_{test}	Failure mode
NGEC	3029.2	3273.9	3015.4	1.08	1.00	Local buckling
NGET	2943.3	3176.9	3056.1	1.08	1.04	Steel yielding
FGEC*	9003.2*	13393.6	11806.2	N.A.	N.A.	Steel yielding & concrete crush
FGET	2990.8	3347.4	3010.5	1.12	1.00	Steel yielding
PGCC	3267.8	3273.9	3322.8	1.00	1.02	Local buckling
PGCT	1204.5	1326.5	1237.0	1.10	1.03	Welding fracture
FGCC*	9008.7*	13393.6	11980.0	N.A.	N.A.	Steel yielding & concrete crush
FGCT	1214.1	1219.4	1183.4	1.00	0.97	Punching shear of end plate
Mean value				1.06	1.01	
Std. dev.				0.05	0.03	

* P_{test} , P_{pre} , and P_{FE} are the maximum loads from the tests, predictions and FE analyses, respectively. The tests of specimens FGEC* and FGCC* are terminated at approximately 9000 kN. $P_{pre_FGEC^*}$ and $P_{pre_FGCC^*}$ are the maximum loads predicted by Eqs. (11)-(13). P_{pre_NGEC} and P_{pre_PGCC} are the maximum loads predicted by Eqs. (4)-(5). P_{pre_NGET} is the maximum load predicted by Eq. (9). P_{pre_FGET} is the maximum load predicted by Eq. (10). P_{pre_PGCT} is the maximum load predicted by Eq. (8). P_{pre_FGCT} is the maximum load predicted by Eqs. (6)-(7).

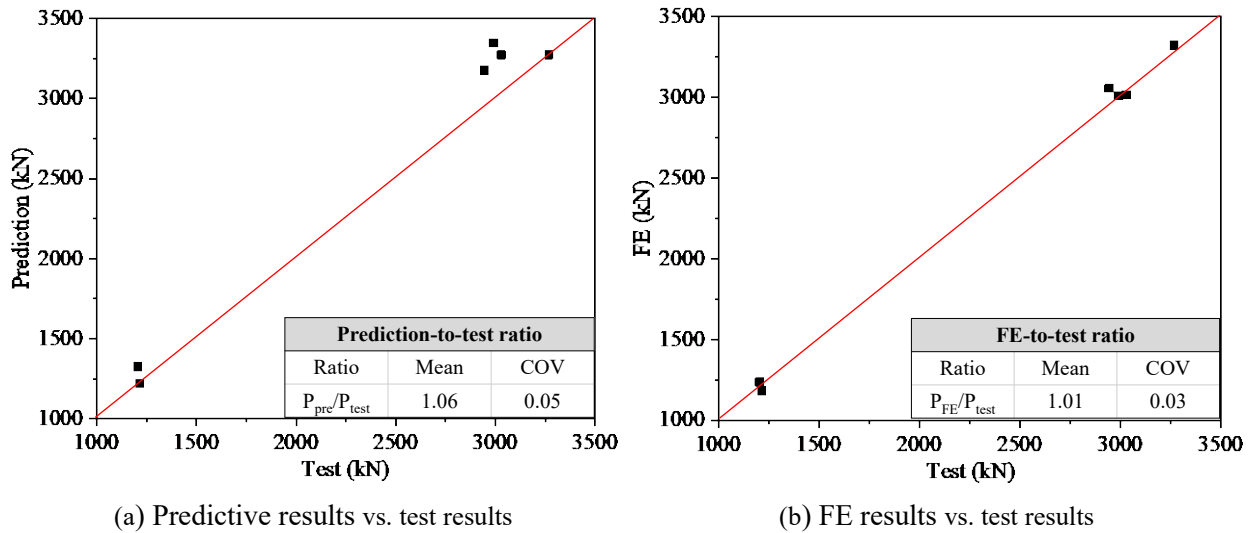


Figure 18. Comparison of the test, FE and predictive results

6. Conclusions

This study develops a novel UHPFRC grouted connection for prefabricated square tubular composite

columns. The load transfer mechanism and the ultimate resistance behaviour of this new connection have been investigated through full-scale experimental tests and FE simulations. This study also evaluates the existing analytical models to predict the ultimate resistance of columns with these novel grouted connections in terms of different failure patterns. The following conclusions are drawn from the study:

- (1) For the connection under tension, three main failure modes are observed from the tests and FE simulations: (i) grout shear damage, (ii) punching shear of the steel end plate or welding fracture and (iii) steel tube yielding. The UHPFRC, which has a higher tensile strength, can provide a strong grouted connection, and the grouted region remains undamaged before the steel tube yields or the weld fails, thereby indicating that the grouted connection is effective in transferring the force from the upper to the lower tube.
- (2) For the connection under compression, two main failure modes are observed from the tests and FE simulations: (i) local buckling of the steel tube and (ii) yielding of the steel tube with concrete crushing. Since the connection has no impact on the vertical compressive load transfer between the upper and lower tubes, the tubes with a grouted connection exhibit a comparable or slightly higher load resistance than those without a grouted connection.
- (3) Three-dimensional FE models incorporated with the CDP model are capable of simulating the compressive and tensile behaviour of the prefabricated columns with grouted connections. The established FE model provides an accurate prediction of the nonlinear load-displacement curves and the failure modes for all the specimens.
- (4) This study evaluates the existing analytical formulas to predict the axial resistance of prefabricated tubes with grouted connections. The accuracy of the formulas in predicting the ultimate resistance is satisfactory when compared with the test results and FE simulations. These analytical formulas can be used in the design of prefabricated tubes with the novel grouted connections.
- (5) This study focuses on the development and fundamental behaviour of the novel grouted connection for prefabricated tubes. Future work is required to study shear failure of the concrete and optimize the geometric parameters and assess seismic performance of these novel grouted connections.

Acknowledgements

The authors would like to acknowledge the research grant received from the National Natural Science Foundation of China (Nos. 51708360, 51978407), the Shenzhen Basic Research Project (No. JCYJ20180305124106675) and the "Country Garden-Shenzhen University Students Innovation and Entrepreneurship Project (No. 000002-24)", which was cooperatively launched by the Belt and Road Research Institute (Shenzhen) for International Cooperation and Development and the Country Garden Holdings.

References

- [1] Mao, C., Shen, Q., Shen, L. and Tang, L. (2013), "Comparative study of greenhouse gas emissions between off-site prefabrication and conventional construction methods: Two case studies of residential projects", *Energy and Buildings*. **66** 165-176.
- [2] Sandanayake, M., Luo, W. and Zhang, G. (2019), "Direct and indirect impact assessment in off-site construction—A case study in China", *Sustainable Cities and Society*. **48** 1-14.
- [3] Arif, M. and Egbu, C. (2010), "Making a case for offsite construction in China", *Engineering, Construction and Architectural Management*. **17**(6), 536-548.
- [4] Mao, C., Xie, F., Hou, L., Wu, P., Wang, J. and Wang, X. (2016), "Cost analysis for sustainable off-site construction based on a multiple-case study in China", *Habitat International*. **57** 215-222.
- [5] Chen, C.C. and Lin, C.C. (2013), "Seismic performance of steel beam-to-column moment connections with tapered beam flanges", *Engineering Structures*. **48** 588-601.
- [6] Gerami, M., Saberli, H., Saberli, V. and Saedi Daryan, A. (2011), "Cyclic behavior of bolted connections with different arrangement of bolts", *Journal of Constructional Steel Research*. **67**(4), 690-705.
- [7] Liu, X.C., Xu, A.X., Zhang, A.L., Ni, Z., Wang, H.X. and Wu, L. (2015), "Static and seismic experiment for welded joints in modularized prefabricated steel structure", *Journal of Constructional Steel Research*. **112** 183-195.
- [8] JGJ1-2014. Technical specification for precast concrete structures. Beijing: China Building Industry Press. 2014.
- [9] Jen Hua Ling, Ahmad Baharuddin Abd. Rahman, Izni Syahrizal Ibrahim, Zuhairi Abdul Hamid. Tensile capacity of grouted splice sleeves[J]. *Engineering Structures*, 2016, 111:285-296.
- [10] Wu Tao, Liu Quan-wei, Cheng Ran, Liu Xi. Experimental study and stress analysis of mechanical performance of grouted sleeve splice. *Engineering Mechanics*. 2017, 34(10):68-75
- [11] Einea A, Yamane T, Tadros M K. Grout-filled pipe splices for precast concrete construction [J]. *PCI Journal*, 1995, 40(1): 82—93.
- [12] Haber Z B, Saiidi M S, Sanders D H. Behavior and simplified modeling of mechanical reinforcing bar splices [J]. *ACI Structural Journal*, 2015, 112(2): 179-188
- [13] Zheng Yongfeng, Guo Zhengxing, Cao Jiang. Confinement mechanism and confining stress distribution of new grouting coupler for rebars splicing. *Journal of Harbin Institute of Technology*. 2015,47(12):106-111.
- [14] ZHENG Yongfeng GUO Zhengxing ZHANG Xin. Effect of sleeve inner cavity structure on bond performance of grouted pipe splice[J].*Journal of Building Structures*,2018,39(09):158-166.
- [15] JGJ107-2016. Technical specification for mechanical splicing of steel reinforcing bars [S]. Beijing: hina building industry press,2016.
- [16] Han, L.-H., He, S.-H. and Liao, F.-Y. (2011), "Performance and calculations of concrete filled steel tubes (CFST) under axial tension", *Journal of Constructional Steel Research*. **67**(11), 1699-1709.
- [17] Billington, C. and Lewis, H. (1978), "The strength of large diameter grouted connections", *Offshore Technology Conference, OTC, Houston*. 291-301.
- [18] Billington, C., (1980) "Research into composite tubular construction for offshore jacket structures", *J Constr Steel Res*. **1**(1), 18-26.

-
- [19] Karsan D and Krahl N. (1985), "Axial strength of grouted pile-to-sleeve connections". *J Struct Eng.* **111**, 889-905.
- [20] Zhao, X.L., Ghojel, J., Grundy, P. and Han, L.H. (2006), "Behaviour of grouted sleeve connections at elevated temperatures", *Thin-Walled Structures.* **44**(7), 751-758.
- [21] Anders, S. and Lohaus, L. (2008), "Optimized high-performance concrete in grouted connections", *Taylor made concrete structures. London: Taylor and Francis Group.* ;396-374.
- [22] Lotsberg, I. (2013), "Structural mechanics for design of grouted connections in monopile wind turbine structures", *Marine Structures.* **32** 113-135.
- [23] Karsan D and Krahl N. (1984), "New API equation for grouted pile to structure connections", *Offshore Technology Conference, OTC, Houston*, 49-56.
- [24] American Petroleum Institute (2000), *Recommended Practice for Planning, Designing and Constructing Fixed Offshore Platforms - Working Stress Design*, 21st edition, Washington.
- [25] Department of Energy (DOE) (1982), "Report of the Working Party on the Strength of Grouted Pile/Sleeve Connections for Offshore Structures". *Offshore Technology Paper*, OTP 11.
- [26] Det Norske Veritas (DNV) (2014), *Offshore Standard, DNV-OS-J101, Offshore Concrete Structures*, Høvik, Norway.
- [27] Det Norske Veritas (DNV) (2016), *Offshore Standard, DNVGL-RP-0419, Analysis of grouted connections using the finite element method*, Høvik, Norway.
- [28] Lee, J.H., Won, D.-H., Jeong, Y.J., Kim, S.H. and Kang, Y.-J. (2017), "Interfacial shear behavior of a high-strength pile to sleeve grouted connection", *Engineering Structures.* **151** 704-723.
- [29] Wang, Z., Zhang, Y., Chen, F., Wang, G., Wang, L. and Jiang, J. (2017), "Axial bearing capacity of large-diameter grouted connections analyzed by means of a simplified double shear test", *Construction and Building Materials.* **134** 245-253.
- [30] Tziavos, N.I., Hemida, H., Metje, N. and Baniotopoulos, C. (2019), "Non-linear finite element analysis of grouted connections for offshore monopile wind turbines", *Ocean Engineering.* **171** 633-645.
- [31] Han, L., Zhao, X. and Tao, Z. (2001), "Tests and mechanics model of concrete-filled SHS stub columns, columns and beam-columns". *Steel & Composite Structures-An International Journal.* **1**(1), 51-74.
- [32] Habel, K., Viviani, M., Denarié, E. and Brühwiler, E. (2006), "Development of the mechanical properties of an Ultra-High Performance Fiber Reinforced Concrete (UHPFRC)", *Cement and Concrete Research.* **36**(7), 1362-1370.
- [33] Kang, S.T., Lee, Y., Park, Y.-D. and Kim, J.-K. (2010), "Tensile fracture properties of an Ultra High Performance Fiber Reinforced Concrete (UHPFRC) with steel fiber", *Composite Structures.* **92**(1), 61-71.
- [34] Kusumawardaningsih, Y., Fehling, E., Ismail, M. and Aboubakr, A.A.M. (2015), "Tensile Strength Behavior of UHPC and UHPFRC", *Procedia Engineering.* **125** 1081-1086.
- [35] Jiang, S.C., Wang, Z. and Zhao, X.L. (2011), "Structural Performance of Prestressed Grouted Pile-to-Sleeve Connections", *Procedia Engineering.* **14** 304-311.
- [36] Li, Z., Chen, T. and Wang, X. (2019), "Behavior of flat grouted connections subjected to lateral pressure and vertical load", *Construction and Building Materials.* **212** 329-341.
- [37] Navaratnam, S., Ngo, T., Gunawardena, T. and Henderson, D. (2019), "Performance Review of Prefabricated

Building Systems and Future Research in Australia", *Buildings*. **9**(2).

- [38] ASTM C1611/C1611-14 (2014), *Standard test method for slump flow of self-consolidating concrete*, West Conshohocken, 568 PA, USA
- [39] Uchida, Y., Tanaka, Y., Katagiri, M. and Niwa, J. (2005), "Outlines of JSCE 'Recommendations for Design and Construction of Ultra High Strength Fiber Reinforced Concrete Structures (Draft)'" , *Concrete Journal*. **43**(3), 3-8.
- [40] Huang, Z., Huang, X., Li, W. and Mei, L. (2019), "Experimental behavior of very high strength concrete encased steel composite column subjected to axial compression and end moment", *Steel and Composite Structures*. **31**(1), 69-83.
- [41] ASTM C39/C39M (2014), *Standard Test Method for Compressive Strength of Cylindrical Concrete Specimens*, West Conshohocken, PA, USA.
- [42] GB/T 31387-2015 (2015). *Reactive powder concrete*, Standardization Administration of China, Beijing, China.
- [43] Concrete Committee JSCE (2008), *Recommendations for Design and Construction of High Performance Fiber Reinforced Cement Composites with Multiple Fine Cracks (HPFRCC)*, Japan.
- [44] ASTM E8/E8M - 15a (2016), *Standard Test Methods for Tension Testing of Metallic Materials1*, West Conshohocken, 568 PA, USA.
- [45] Lee, J. and Fenves, G.L., (1998). "Plastic-damage model for cyclic loading of concrete structures", *J. Eng.* **124** (8) 892-900.
- [46] Yu, T., Teng, J.G., Wong, Y.L. and Dong, S.L. (2010), "Finite element modeling of confined concrete-II: Plastic-damage model", *Engineering Structures*. **32**(3), 680-691.
- [47] Krahl, P.A., Carrazedo, R. and El Debs, M.K. (2018), "Mechanical damage evolution in UHPFRC: Experimental and numerical investigation", *Engineering Structures*. **170** 63-77.
- [48] Huang, Z. and Liew, J.Y.R. (2015), "Nonlinear finite element modelling and parametric study of curved steel–concrete–steel double skin composite panels infilled with ultra-lightweight cement composite", *Construction and Building Materials*. **95**, 922-938.
- [49] GB 50010-2010 (2015). Code for design of concrete structures, Standardization Administration of China, Beijing, China.
- [50] Guo, X.Y., Kang J.F. and Zhu, J.S. (2017), "Constitutive relationship of ultrahigh performance concrete under uniaxial compression", *journal of southeast university (Natural Science Edition)*. **47**(2), 369-376. (in Chinese)
- [51] Wille, K., Kim, D. and Naaman E. (2011)"Strain-hardening UHP-FRC with low fiber contents", *Materials and Structures*. **44**(3), 583-598.
- [52] Gribniak, V., Kaklauskas, G., Hung Kwan, A.K., Bacinskas, D. and Ulbinas, D. (2012), "Deriving stress–strain relationships for steel fibre concrete in tension from tests of beams with ordinary reinforcement", *Engineering Structures*. **42** 387-395.
- [53] Hameed, R., Sellier, A., Turatsinze, A. and Duprat, F. (2013), "Metallic fiber-reinforced concrete behaviour: Experiments and constitutive law for finite element modeling", *Engineering Fracture Mechanics*. **103** 124-131.

-
- [54] Nie, J.G. and Wang, Y.H. (2013), "Comparison study of constitutive model of concrete in ABAQUS for static analysis of structures", *Engineering Mechanics*. **30**(4), 59-67.
- [55] Birtel, V. and Mark P. (2006), "Parameterised Finite Element Modelling of RC Beam Shear Failure", *ABAQUS Users' Conference*. 95-108.
- [56] Chi, Y., Yu, M., Huang, L. and Xu, L. (2017), "Finite element modeling of steel-polypropylene hybrid fiber reinforced concrete using modified concrete damaged plasticity", *Engineering Structures*. 148 23-35.
- [57] Eurocode 3 (2005), *Design of steel structures, European Committee for Standardisation*, Brussels, Belgium.
- [58] Packer, J. and Henderson, J. (1997), "Hollow structural section connections and trusses—A design guide (2nd ed)", *Canadian Institute of Steel Construction*, Toronto, Canada.
- [59] Eurocode 4 (2004), *Design of composite steel and concrete structures, European Committee for Standardisation*, Brussels, Belgium.